

# A Note on Kinematic Flow and Differential Equations for Two-Site One-Loop Graph in FRW Spacetime

---

Yanfeng Hang,<sup>a</sup> Cong Shen<sup>a</sup>

<sup>a</sup>*Department of Physics and Astronomy,  
Northwestern University, Evanston, IL 60208, USA*

*E-mail:* [yfhang@northwestern.edu](mailto:yfhang@northwestern.edu), [CongShen2028@u.northwestern.edu](mailto:CongShen2028@u.northwestern.edu)

ABSTRACT: In this work, we investigate the canonical differential equations dictate the behavior of cosmological wavefunction coefficients for two-site loop-level configurations in conformally-coupled scalar field theory within a general power-law FRW cosmology. Employing the tools of relative twisted cohomology and integration-by-parts techniques, we systematically derive these equations, thereby establishing a comprehensive framework for loop-level correlators for the first time. A novel contribution of this work is the extension of kinematic flow framework to the loop-level scenarios. Using a graphical approach based on family trees generated by marked tubing graphs, we efficiently construct the differential equations while capturing the singularity structure and hierarchical relationships within the associated integral families. Furthermore, we present new insights into the tadpole systems, uncovering that their integral families can exhibit multiple parent functions due to distinct, non-overlapping relative hyperplanes, in contrast with the single parent function of bubble and tree-level systems. Additionally, we demonstrate that tadpole wavefunction coefficients selectively probe only a subset of the cohomology space, despite the hyperplane arrangement suggesting a higher-dimensional structure. Beyond these findings, we provide a preliminary discussion on generalization to two-site higher-loop configurations, laying the groundwork for future exploration of more intricate scenarios. This work introduces several first-time methodologies and results, advancing our understanding of the geometric, topological, and dynamical properties of loop-level wavefunction coefficients and offering new insights for probing the fundamental mechanisms of the early universe.

arXiv:2410.17192 [hep-th]

---

## Contents

<b>1</b>	<b>Introduction</b>	<b>1</b>
<b>2</b>	<b>Toy Model and Cosmological Wavefunction Coefficients</b>	<b>3</b>
<b>3</b>	<b>Two-Site One-Loop Wavefunction Coefficients and Canonical DEs</b>	<b>6</b>
3.1	Two-Site One-Loop Bubble	6
3.1.1	Hyperplane Arrangements	7
3.1.2	Derivation of Canonical DEs	10
3.2	Two-Site One-Loop Tadpole	15
3.2.1	Hyperplane Arrangements and Derivation of Canonical DEs	16
3.2.2	New Features from Tadpole System and Triangle Basis	18
<b>4</b>	<b>Kinematic Flow for Two-Site One-Loop Graph</b>	<b>24</b>
4.1	Two-Site One-Loop Bubble	24
4.2	Two-Site One-Loop Tadpole	31
<b>5</b>	<b>Analysis for Two-Site Higher Loop Graph</b>	<b>35</b>
<b>6</b>	<b>Conclusion and Outlook</b>	<b>42</b>
<b>A</b>	<b>The Derivation of Two-Site One-Loop DEs from IBP</b>	<b>43</b>
A.1	Two-Site One-Loop Bubble	43
A.2	Two-Site One-Loop Tadpole	45
<b>B</b>	<b>Tubings of Two-Site Two-Loop Bubble System</b>	<b>46</b>

---

## 1 Introduction

The study of cosmological dynamics has emerged as a central focus in modern theoretical physics, especially in understanding the early universe and the mechanisms that shaped its evolution. Among the many toy models, the investigation of wavefunction coefficients for conformally-coupled scalar theory in a power-law Friedmann-Robertson-Walker (FRW) universe [1, 2] has proven instrumental in advancing our understanding of cosmological processes. These wavefunction coefficients encapsulate key information about the inflationary dynamics and the generation of primordial fluctuations, serving as a bridge between theoretical models and observational cosmology.

In recent years, various innovative methods have been developed to compute and study cosmological correlators, unveiling new mathematical structures and offering deeper insights into the nature of the early universe. Notable approaches include: The framework

of the cosmological polytope [1–4], which geometrically encodes the combinatorial and analytic properties of correlators; The techniques based on relative twisted cohomology/dual cohomology, intersection theory and algebraic geometry [5, 6], which comprehensively study the differentiation system of FRW wavefunction coefficients at both tree and loop level; The kinematic flow method [7, 8], which organizes the canonical differential equations of tree-level FRW wavefunctions coefficients based on the hierarchical structure of their singularities represented by tubing graphs.

In this work, we focus on the loop-level wavefunction coefficients in conformally-coupled scalar field theory with non-conformal polynomial interactions in a general power-law FRW universe. We utilize relative twisted cohomology [9–11] alongside the integration-by-parts (IBP) to derive the canonical differential equations (DEs) [12, 13] associated with the wavefunction coefficients of two-site one-loop diagrams, and based on the analysis of one-loop case, we provide a concise discussion extending to two-site two-loop and arbitrary-loop scenarios. A key component of our study is the application and extension of the kinematic flow framework to loop level. This powerful methodology enables the systematic prediction of canonical differential equations by representing the singularities of the system as marked tubing graphs [7, 8, 14–16]. These graphs encode the hierarchical relationships among the integrals, forming family trees that organize the system’s structure according to some simple rules. By utilizing this framework, we streamline the derivation of differential equations from the family trees constructed by the tubing graphs.

Another important point is our analysis of the hyperplane arrangement for the tadpole system. We discover that its integral families can contain more than one parent function, a result of distinct, non-overlapping relative hyperplanes, which stands in contrast to the single parent function observed in bubble and tree-level cases. Moreover, an intriguing feature of the tadpole wavefunction coefficient is its selective involvement with the system: only a subset of basis functions contributes to the canonical differential equations, despite the hyperplane arrangement suggesting a higher-dimensional vector space. These findings are presented for the first time in this work.

As this paper was being finalized, we found Ref. [17] also investigated the differential equations for cosmological loop integrands but employed a different methodology. While our approach differs from theirs, we find agreement with their results and view their findings as complementary to our work.

This paper is organized as follows: In Section 2, we set up the model of conformally-coupled scalars in the general power-law FRW background and provide a brief review of the cosmological wavefunction coefficients. In Section 3, we systematically analyze the two-site one-loop FRW wavefunction coefficients of bubble and tadpole types using the framework of relative twisted cohomology and hyperplane arrangements. We perform a detailed study of the canonical forms associated with the integral family, investigating their structure within the bounded chambers, and derive the corresponding canonical differential equations. This derivation relies on matching residues at different codimension-2 boundaries using IBP techniques. Further, we show that at the tadpole loop level, parent function is not unique, requiring two parent functions for the tadpole system. This contrasts with the unique parent

function in tree level and in bubble systems, where multiple parent function can merge into a single function. In Section 4, we present the extension of kinematic flow framework from tree-level to loop-level computations for the first time. Singularities in the differential system are represented as the marked tubing graphs, establishing a direct correspondence between these graphical structures and the canonical differential equations. Following the simple rules, the differential equations can be directly constructed from the family trees generated by the evolution of marked tubes. In Section 5, we provide four examples of wavefunction coefficients for two-site two-loop bubble and tadpole diagrams, exploring the configurations of their hyperplane arrangements based on the analysis of one-loop cases. We also examine the feasibility of extending the kinematic flow method to scenarios beyond one-loop. Finally, in Section 6, we summarize our results and discuss potential directions for future research. The Appendices will provide additional details that are missing from the main text.

## 2 Toy Model and Cosmological Wavefunction Coefficients

We consider the model of conformally-coupled scalar fields with a non-conformal polynomial self-interaction term in a general metric for the Friedmann-Robertson-Walker (FRW) universe. The relevant action defined in a  $(d + 1)$ -dimensional spacetime can be expressed as follows:

$$S_{\text{FRW}} = - \int d^d x \int_{-\infty}^0 d\eta \sqrt{-g} \left[ \frac{1}{2} g^{\alpha\beta} \partial_\alpha \phi \partial_\beta \phi + \left( \frac{d-1}{8d} \right) R \phi^2 + \sum_{n \geq 3} \frac{\lambda_n}{n!} \phi^n \right], \quad (2.1)$$

where  $\eta$  denotes the conformal time,  $R$  refers to the Ricci scalar and  $\lambda_n$  is the coupling constant. The FRW metric is defined as follows:

$$ds^2 = g_{\alpha\beta} dx^\alpha dx^\beta = [a(\eta)]^2 (-d\eta^2 + \delta_{ij} dx^i dx^j), \quad (2.2)$$

where  $a(\eta)$  represents the scale factor and the indices  $\{i, j\} = 1, \dots, d$  span the spatial dimensions. Further, by substituting FRW metric (2.2) into the action (2.1) and rescaling the scalar field  $\phi \rightarrow [a(\eta)]^{(1-d)/2} \phi$ , the FRW action (2.1) will reduce to the action describing massless scalar fields effectively in a  $(d + 1)$ -dimensional Minkowski (flat) spacetime:

$$S_{\text{Mink}}^{\text{eff}} = - \int d^d x \int_{-\infty}^0 d\eta \left[ \frac{1}{2} (\partial\phi)^2 + \sum_{n \geq 3} \frac{\lambda_n(\eta)}{n!} \phi^n \right], \quad (2.3)$$

where the time-dependent coupling  $\lambda_n(\eta)$  is defined as follows:

$$\lambda_n(\eta) \equiv \lambda_n [a(\eta)]^{2-(n-2)(d-1)/2} = \lambda_n \eta^{-(1+\varepsilon)(2-(n-2)(d-1)/2)}, \quad (2.4)$$

where the final equality holds when the scale factor takes the power-law form (2.10), as will be discussed later.

Next, we provide a brief review of the cosmological wavefunction coefficients. These coefficients describe the amplitude for different configurations of fields in the early universe

and encode crucial information about cosmological fluctuations. It can be derived from the path integral formalism, where the wavefunction  $\Psi[\phi]$  is obtained by summing over all possible field configurations in a given cosmological background. Specifically, we can express the cosmological wavefunction  $\Psi[\phi]$  as a path integral over the field configurations with boundary conditions:

$$\Psi[\phi] = \int_{\varphi[-\infty(1-i\epsilon)]=0}^{\varphi(0)=\phi} \mathcal{D}\varphi e^{iS[\varphi]}, \quad (2.5)$$

where  $S[\varphi]$  is the action of the field  $\varphi$  as given in Eq. (2.3) and the integral is performed over all field configurations. And, the  $i\epsilon$ -prescription is crucial for suppressing the negative-frequency component and ensuring that the initial state corresponds to a pure, minimal-energy (Bunch-Davies) vacuum at the early time  $\eta \rightarrow -\infty$ . Further,  $|\Psi[\phi]|^2$  provides the physical meaning of the probability density for spatial field configurations. Thus, the equal-time  $m$ -point correlation function for  $\phi$  can be written as:

$$\langle \phi(\mathbf{x}_1) \cdots \phi(\mathbf{x}_m) \rangle = \int \mathcal{D}\phi \phi(\mathbf{x}_1) \cdots \phi(\mathbf{x}_m) |\Psi[\phi]|^2. \quad (2.6)$$

The wavefunction can also be expanded in terms of its coefficients, which are related to cosmological correlation functions. For example, expanding  $\Psi[\phi]$  perturbatively gives:

$$\Psi[\phi] = \exp \left\{ - \sum_{m \geq 2} \frac{1}{m!} \int \prod_{i=1}^m \left[ \frac{d^d \mathbf{k}_i}{(2\pi)^d} \phi_{\mathbf{k}_i} \right] \psi_m(\mathbf{k}) (2\pi)^d \delta^{(d)} \left( \sum_{j=1}^m \mathbf{k}_j \right) \right\}, \quad (2.7)$$

where  $\mathbf{k} \equiv \{\mathbf{k}_1, \dots, \mathbf{k}_m\}$  and we refer  $\psi_m(\mathbf{k})$  as the cosmological wavefunction coefficients, encoding the interactions between  $m$ -point fluctuations of the field.

The path integral can be performed diagrammatically in the usual way with Feynman graphs. Each diagram corresponds to a specific contribution to the perturbative expansion of the wavefunction, which can be calculated by using the following Feynman rules: (i). Draw the boundary surface at fixed time  $\eta = 0$  where the wavefunction will be computed and draw all diagrams ending on the boundary surface. (ii). Attach a vertex factor  $iV_v$  to each bulk interaction, where  $V_v$  is defined by the interaction terms in the action. For a scalar field with non-derivative polynomial interactions as given in Eq. (2.3),  $V_v$  depends only on the coupling constant. (iii). Assign a bulk-to-boundary propagator,  $K(E; \eta)$ , to each external line. For a given vertex  $v$ , this propagator corresponds to the propagation of a field from a bulk vertex to the late-time boundary, and it takes the form:

$$K_v(E_v; \eta_v) = e^{iE_v \eta_v}, \quad (2.8)$$

where  $E_v = \sum_i |\mathbf{k}_i|$  denotes the sum of the energies of all  $i$  external legs connected to the vertex  $v$ . (iv). Assign a bulk-to-bulk propagator,  $G(E; \eta, \eta')$ , to each internal line. For an internal line  $e$  connecting two vertices,  $v_e$  and  $v'_e$ , the bulk-to-bulk propagator  $G_e(E_e; \eta_{v_e}, \eta_{v'_e})$  describes the propagation of fields between two vertices  $v_e$  and  $v'_e$  located at different times and it takes the form:

$$G_e(E_e; \eta_{v_e}, \eta_{v'_e}) = \frac{1}{2E_e} \left[ e^{-iE_e(\eta_{v_e} - \eta_{v'_e})} \theta(\eta_{v_e} - \eta_{v'_e}) + e^{iE_e(\eta_{v_e} - \eta_{v'_e})} \theta(\eta_{v'_e} - \eta_{v_e}) - e^{iE_e(\eta_{v_e} + \eta_{v'_e})} \right], \quad (2.9)$$

where  $E_e = |\mathbf{k}_e|$  represent the energy of an internal line  $e$ . (v). Integrate over the time insertions of all bulk vertices and any loop momenta<sup>1</sup>.

Finally, we assume that the scale factor  $a(\eta)$  appearing in the FRW metric (2.2) takes the following power-law form [5, 7, 8]:

$$a(\eta) = \frac{1}{\eta^{1+\varepsilon}}, \quad (2.10)$$

where the parameter  $\varepsilon = 0, -1, -2, -3$  corresponding to the de Sitter (dS), flat, radiation- and matter-dominated universe, respectively. Thus, in the case of a power-law form (2.10), we can analyze and compute the wavefunction coefficient. The corresponding Feynman rules need slight modifications, where the bulk-to-boundary propagator (2.8) and bulk-to-bulk propagator (2.9) remain unchanged from their flat-space forms. As for the vertices, the  $n$ -point time-dependent coupling (2.4) can be expressed in the energy space via following Mellin transform:

$$\lambda_n(\eta) = \lambda_n \eta^{-\gamma} = \int_0^{+\infty(1-i\epsilon)} dx \bar{\lambda}_n(x) e^{ix\eta}, \quad (2.11)$$

where  $\gamma = (1 + \varepsilon)[2 - (n - 2)(d - 1)/2]$  and the energy-dependent coupling constant  $\bar{\lambda}_n(x)$  is given by

$$\bar{\lambda}_n(x) = \lambda_n \frac{e^{-i\pi\gamma/2}}{\Gamma(\gamma)} x^{\gamma-1}. \quad (2.12)$$

Further, the  $i\epsilon$ -prescription modifies the integration contour in the complex plane to ensure convergence of the integral at large  $x$ .

Therefore, for a given  $N$ -site  $L$ -loop graph characterized by the vertex set  $\mathcal{V}$  and edge set  $\mathcal{E}$ , its FRW wavefunction coefficient can be obtained by appropriately shifting the flat-space expression over the external energies:

$$\psi_{(N,L)}^{\text{FRW}}(X_v, Y_e) = \int_0^{+\infty} \prod_{v \in \mathcal{V}} [dx_v \bar{\lambda}_n(x_v)] \tilde{\psi}_{(N,L)}^{\text{Mink}}(X_v + x_v, Y_e), \quad (2.13)$$

where  $X_v$  represents the total energy flowing from a vertex  $v$  to the late-time boundary and  $Y_e$  corresponds to the energy of each internal line  $e$ . In Eq. (2.13), the integral involving the power parameter  $\gamma$  is valid for  $\gamma > 0$  in  $\bar{\lambda}_n(x_v)$ , while for  $\gamma \leq 0$ , the integration over  $x$  can be replaced by a differential operator acting on  $\tilde{\psi}_{(N,L)}^{\text{Mink}}$  [4]. Further, the flat-space wavefunction coefficient integrand  $\tilde{\psi}_{(N,L)}^{\text{Mink}}$  is derived as follows:

$$\tilde{\psi}_{(N,L)}^{\text{Mink}}(X_v, Y_e) = i^N \int_{-\infty}^0 \prod_{v \in \mathcal{V}} d\eta_v K_v(X_v; \eta_v) \prod_{e \in \mathcal{E}} G_e(Y_e; \eta_{v_e}, \eta_{v'_e}), \quad (2.14)$$

where the bulk-to-boundary propagator  $K_v$  and bulk-to-bulk propagator  $G_e$  are defined in Eqs. (2.8)-(2.9). Finally, for convenience, we will drop out the superscripts ‘‘FRW’’ and ‘‘Mink’’ and use  $\psi_{(N,L)}$  and  $\tilde{\psi}_{(N,L)}$  to denote the wavefunction coefficients in FRW and flat spacetimes in the following discussion.

---

<sup>1</sup>In this analysis, we focus solely on the wavefunction coefficient at the integrand level, without performing integration over loop momenta.

### 3 Two-Site One-Loop Wavefunction Coefficients and Canonical DEs

In this section, we investigate a detailed analysis of the two-site one-loop wavefunction coefficients of the bubble and tadpole diagrams within a  $(d + 1)$ -dimensional power-law FRW universe. For the first time, we systematically find the corresponding integral basis associated with the loop-level wavefunction coefficients guided by the structure of the hyperplane arrangements. Furthermore, we also provide the comprehensive derivations for the canonical differential equations, employing integration-by-parts (IBP) techniques to capture their intricate dependencies.

#### 3.1 Two-Site One-Loop Bubble

We first consider the two-site one-loop bubble-type wavefunction coefficient whose Feynman diagram is shown in Fig. 1. Following the Feynman rules given in Section 2, we can compute the flat-space wavefunction coefficient as follows:

$$\begin{aligned} \tilde{\psi}_{(2,1)}^{\text{bub}} &= i^2 \int_{-\infty}^0 d\eta_1 \int_{-\infty}^0 d\eta_2 K_1(X_1; \eta_1) K_2(X_2; \eta_2) G_1(Y_1; \eta_1, \eta_2) G_2(Y_2; \eta_2, \eta_1) \\ &= \frac{2(X_1 + X_2 + Y_1 + Y_2)}{(X_1 + X_2)(X_1 + X_2 + 2Y_1)(X_1 + X_2 + 2Y_2)(X_1 + Y_1 + Y_2)(X_2 + Y_1 + Y_2)}. \end{aligned} \quad (3.1)$$

Then, to derive the two-site one-loop wavefunction coefficient in a general FRW universe, we can shift over the external energies of its corresponding flat-space form (3.1) via the following transformations:  $(X_1, X_2) \rightarrow (X_1 + x_1, X_2 + x_2)$ . Further, we incorporate a twist term  $(x_1 x_2)^{\gamma-1}$  to regularize the integrand. Specifically, we focus on the case  $\gamma = 1 + \varepsilon$ , where the twister parameter  $\varepsilon$  effectively controls and mitigates the singular behavior. Thus, the complete FRW wavefunction coefficient for two-site one-loop bubble diagram is derived in the following integration representation:

$$\psi_{(2,1)}^{\text{bub}} = 4Y_1 Y_2 \frac{\lambda_n^2 (-1)^{1+\varepsilon}}{[\Gamma(1+\varepsilon)]^2} \int dx_1 \wedge dx_2 (x_1 x_2)^\varepsilon \tilde{\psi}_{(2,1)}^{\text{bub}} \Big|_{X_1 \rightarrow X_1 + x_1}^{X_2 \rightarrow X_2 + x_2}, \quad (3.2)$$

where and we have also included an overall factor  $4Y_1 Y_2$  for later convenience. Moreover, from now on and in all subsequent examples, we will ignore the overall common factor  $\lambda_n^2 (-1)^{1+\varepsilon} / [\Gamma(1 + \varepsilon)]^2$  appearing in all FRW wavefunction coefficients.

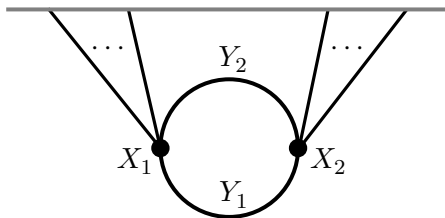


**Figure 1.** The Feynman diagram for the two-site one-loop bubble-type wavefunction coefficient, where  $\{X_1, X_2\}$  are associated with the sum of energies flowing from the vertices to the late-time boundary and  $\{Y_1, Y_2\}$  represent the energies of the internal lines.

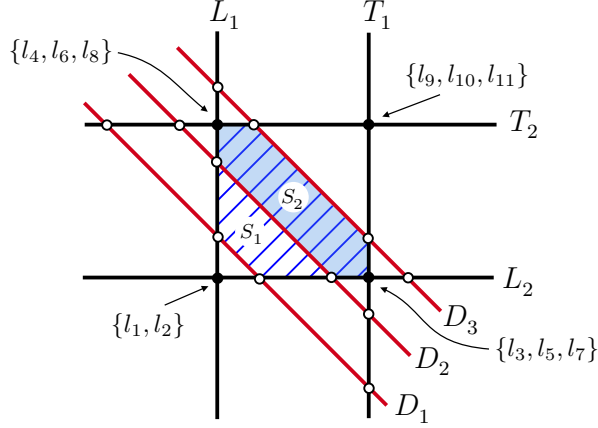


**Figure 2.** The complete hyperplane arrangement associated with the two-site one-loop bubble-type wavefunction coefficient. All black and white intersection points represent the codimension-2 boundaries. Among these, the four points  $L_1 \cap L_2$ ,  $L_1 \cap T_2$ ,  $L_2 \cap T_1$  and  $T_1 \cap T_2$  are specifically used to calculate the letters  $\{l_i\}$  in our chosen basis.

### 3.1.1 Hyperplane Arrangements

While the integrals in Eq. (3.2) can be computed directly, a more efficient and elegant approach leverages advanced mathematical tools. Specifically, we employ concepts from intersection theory and twisted cohomology [9–11] in conjunction with the method of canonical differential equations [12, 13] to evaluate Eq. (3.2). This allows us to reformulate the two-site one-loop FRW wavefunction coefficient (3.2) as follows:

$$\psi_{(2,1)}^{\text{bub}} = \int dx_1 \wedge dx_2 (T_1 T_2)^\varepsilon \left[ \frac{4Y_1 Y_2}{L_1 L_2 D_3} \left( \frac{1}{D_1} + \frac{1}{D_2} \right) \right] \equiv \int (T_1 T_2)^\varepsilon \Omega_{\mathcal{P}}^2. \quad (3.3)$$

In Eq. (3.3), we have defined:

$$\begin{aligned} T_1 &= x_1, & T_2 &= x_2, \\ L_1 &= x_1 + X_1 + Y_1 + Y_2, & L_2 &= x_2 + X_2 + Y_1 + Y_2, \\ D_1 &= x_1 + x_2 + X_1 + X_2 + 2Y_1, & D_2 &= x_1 + x_2 + X_1 + X_2 + 2Y_2, \\ D_3 &= x_1 + x_2 + X_1 + X_2, \end{aligned} \quad (3.4)$$

where those divisors are expressed in the linear form, corresponding to seven independent hyperplanes determined by the equations:  $\{T_i, L_j, D_k\} = 0$ . Their geometric arrangement in  $(x_1, x_2)$ -coordinate system is illustrated in Fig. 2. Further, inspecting Eq. (3.3), the extra normalization factor  $4Y_1 Y_2$  is included in order to ensure that the canonical 2-form  $\Omega_{\mathcal{P}}^2$  has the residues of  $\pm 1$  on all codimension-2 boundaries [18]. Moreover, the branch planes  $\{T_1, T_2\}$  correspond to twisted singularities or “mild” singularities, regulated by the parameter  $\varepsilon$ , while the hyperplanes  $\{L_i, D_j\}$  are associated with the relative singularities or “dangerous” singularities of the integrand [5]. The overall analytic structure of these integrals is fundamentally governed by the intersections of the surfaces  $\{T_i, L_j, D_k\}$ , as these intersections dictate the behavior and singularities of the whole system.



As discussed in Refs. [9–11], the number of independent master integrals is equal to the number of chambers bounded by the hyperplanes (3.4). For the first time, our detailed analysis reveals that Fig. 2 can be partitioned into three distinct subsystems of hyperplane arrangements in the two-site one-loop level. Each subsystem shares four common hyperplanes  $\{T_1, T_2, L_1, L_2\}$ , and contains one unique diagonally-placed hyperplane  $\{D_1, D_2, D_3\}$ . Consequently, Fig. 2 encompasses a total of twelve bounded chambers, each corresponding to an independent canonical form. These forms are represented as triangles arising from the intersections of hyperplanes, consistent with the framework outlined in Ref. [18]. And based on this foundation, Refs. [7, 8] demonstrate that each chamber uniquely maps to a specific wavefunction coefficient. Therefore, within each subsystem of hyperplanes, there exists a hierarchical structure of functions comprising a “parent” function  $\mathcal{P}_i$  accompanied by three “decedent” functions:  $\mathcal{F}_i$ ,  $\tilde{\mathcal{F}}_i$  and  $\mathcal{Q}_i$ . These twelve functions collectively form three sets:

$$\mathbf{F}_i \equiv \{ \mathcal{P}_i, \mathcal{F}_i, \tilde{\mathcal{F}}_i, \mathcal{Q}_i \}, \quad i = 1, 2, 3, \quad (3.5)$$

where each function is associated with a bounded triangle region, which is systematically defined as follows:

$$\text{Layer-0: } \triangle_{L_1 L_2 D_i} \longleftrightarrow \mathcal{P}_i = \int (T_1 T_2)^\varepsilon \left( \text{dlog} \frac{L_1}{D_i} \wedge \text{dlog} \frac{L_2}{D_i} \right) \equiv \int \text{d}\mu \bar{\Omega}_{\mathcal{P}_i}, \quad (3.6a)$$

$$\text{Layer-1: } \triangle_{T_1 L_2 D_i} \longleftrightarrow \mathcal{F}_i = \int (T_1 T_2)^\varepsilon \left( \text{dlog} \frac{T_1}{D_i} \wedge \text{dlog} \frac{L_2}{D_i} \right) \equiv \int \text{d}\mu \bar{\Omega}_{\mathcal{F}_i}, \quad (3.6b)$$

$$\triangle_{L_1 T_2 D_i} \longleftrightarrow \tilde{\mathcal{F}}_i = \int (T_1 T_2)^\varepsilon \left( \text{dlog} \frac{L_1}{D_i} \wedge \text{dlog} \frac{T_2}{D_i} \right) \equiv \int \text{d}\mu \bar{\Omega}_{\tilde{\mathcal{F}}_i}, \quad (3.6c)$$

$$\text{Layer-2: } \triangle_{T_1 T_2 D_i} \longleftrightarrow \mathcal{Q}_i = \int (T_1 T_2)^\varepsilon \left( \text{dlog} \frac{T_1}{D_i} \wedge \text{dlog} \frac{T_2}{D_i} \right) \equiv \int \text{d}\mu \bar{\Omega}_{\mathcal{Q}_i}, \quad (3.6d)$$

where we have re-defined the canonical forms as:  $\Omega \equiv \bar{\Omega} dx_1 \wedge dx_2$ <sup>2</sup>, and further combined  $dx_1 \wedge dx_2$  with the prefactor  $(T_1 T_2)^\varepsilon$  into a compact measure form:  $\text{d}\mu \equiv (T_1 T_2)^\varepsilon dx_1 \wedge dx_2$ . To avoid confusion, we will hereafter refer to the coefficient  $\bar{\Omega}$  as the canonical form. Then, we derive those canonical forms as follows:

$$\text{Layer-0: } \bar{\Omega}_{\mathcal{P}_1} = \frac{-2Y_2}{L_1 L_2 D_1}, \quad \bar{\Omega}_{\mathcal{P}_2} = \frac{-2Y_1}{L_1 L_2 D_2}, \quad \bar{\Omega}_{\mathcal{P}_3} = \frac{-2(Y_1 + Y_2)}{L_1 L_2 D_3}, \quad (3.7a)$$

$$\text{Layer-1: } \bar{\Omega}_{\mathcal{F}_1} = \frac{X_1 + Y_1 - Y_2}{T_1 L_2 D_1}, \quad \bar{\Omega}_{\mathcal{F}_2} = \frac{X_1 - Y_1 + Y_2}{T_1 L_2 D_2}, \quad \bar{\Omega}_{\mathcal{F}_3} = \frac{X_1 - Y_1 - Y_2}{T_1 L_2 D_3}, \quad (3.7b)$$

$$\bar{\Omega}_{\tilde{\mathcal{F}}_1} = \frac{X_2 + Y_1 - Y_2}{T_2 L_1 D_1}, \quad \bar{\Omega}_{\tilde{\mathcal{F}}_2} = \frac{X_2 - Y_1 + Y_2}{T_2 L_1 D_2}, \quad \bar{\Omega}_{\tilde{\mathcal{F}}_3} = \frac{X_2 - Y_1 - Y_2}{T_2 L_1 D_3}, \quad (3.7c)$$

$$\text{Layer-2: } \bar{\Omega}_{\mathcal{Q}_1} = \frac{X_1 + X_2 + 2Y_1}{T_1 T_2 D_1}, \quad \bar{\Omega}_{\mathcal{Q}_2} = \frac{X_1 + X_2 + 2Y_2}{T_1 T_2 D_2}, \quad \bar{\Omega}_{\mathcal{Q}_3} = \frac{X_1 + X_2}{T_1 T_2 D_3}. \quad (3.7d)$$

Specifically, we define canonical forms with a positively oriented convention, ensuring that the aforementioned  $\bar{\Omega}$  are positive within the corresponding bounded region. In Eqs. (3.6)–(3.7), we have categorized functions/forms into three layers:

<sup>2</sup>For simplicity, from now to the following discussions, we will omit the superscript “2” of the canonical 2-form  $\Omega^2$ .

- Layer-0: Functions in this layer do not involve any of the twist planes  $T_1$  and  $T_2$ .
- Layer-1: Functions in this layer are obtained by replacing the  $L_1$ - or  $L_2$ -plane in the corresponding layer-0 functions with the twist planes  $T_1$  or  $T_2$ . For example,  $\mathcal{F}_i, \tilde{\mathcal{F}}_i$  can be derived from the parent function as  $\mathcal{F}_i = \mathcal{P}_i|_{L_1 \rightarrow T_1}$ ,  $\tilde{\mathcal{F}}_i = \mathcal{P}_i|_{L_2 \rightarrow T_2}$ .
- Layer-2: Functions in this layer are derived by further replacing the remaining  $L_1$ - or  $L_2$ -plane in the corresponding layer-1 functions with the twist planes  $T_1$  or  $T_2$  i.e.,  $Q_i = \mathcal{F}_i|_{L_2 \rightarrow T_2} = \tilde{\mathcal{F}}_i|_{L_1 \rightarrow T_1}$ .

Further, each set  $\mathbf{F}_i$  defined in Eq. (3.5) contains four members, each corresponding to a canonical 2-form uniquely associated with a codimension-2 boundary, represented by the four black intersection points shown in Fig. 2. Thus, for each set of  $\mathbf{F}_i$ , any form can be decomposed into this basis by matching residues at these distinctive intersection points, which correspond to the dlog singularities of the form.

However, analyzing the hyperplane arrangement reveals that the twelve chambers (triangles) are not independent, they are subject to two linear constraints, which can be expressed as follows:

$$\begin{aligned} S_1 &= \Delta_{T_1 T_2 D_1} - \Delta_{L_1 T_2 D_1} - \Delta_{L_2 T_1 D_1} - \Delta_{T_1 T_2 D_3} \\ &= \Delta_{L_1 L_2 D_3} - \Delta_{L_1 T_2 D_3} - \Delta_{L_2 T_1 D_3} - \Delta_{L_1 L_2 D_1}, \end{aligned} \quad (3.8a)$$

$$\begin{aligned} S_2 &= \Delta_{T_1 T_2 D_2} - \Delta_{L_1 T_2 D_2} - \Delta_{L_2 T_1 D_2} - \Delta_{T_1 T_2 D_3} \\ &= \Delta_{L_1 L_2 D_3} - \Delta_{L_1 T_2 D_3} - \Delta_{L_2 T_1 D_3} - \Delta_{L_1 L_2 D_2}, \end{aligned} \quad (3.8b)$$

where  $S_1$  and  $S_2$  are correspond to the blue-shaded and blue hexagonal regions in Fig. 2, respectively. Each region can be constructed by stitching together several triangles defined earlier, with two distinct ways of assembling them. Therefore, with a consistent choice of orientation, the constraints (3.8) induce two linear relations among the canonical forms:

$$\bar{\Omega}_{Q_1} - \bar{\Omega}_{\tilde{\mathcal{F}}_1} - \bar{\Omega}_{\mathcal{F}_1} - \bar{\Omega}_{Q_3} = \bar{\Omega}_{\mathcal{P}_3} - \bar{\Omega}_{\tilde{\mathcal{F}}_3} - \bar{\Omega}_{\mathcal{F}_3} - \bar{\Omega}_{\mathcal{P}_1}, \quad (3.9a)$$

$$\bar{\Omega}_{Q_2} - \bar{\Omega}_{\tilde{\mathcal{F}}_2} - \bar{\Omega}_{\mathcal{F}_2} - \bar{\Omega}_{Q_3} = \bar{\Omega}_{\mathcal{P}_3} - \bar{\Omega}_{\tilde{\mathcal{F}}_3} - \bar{\Omega}_{\mathcal{F}_3} - \bar{\Omega}_{\mathcal{P}_2}, \quad (3.9b)$$

where these conditions reduce the total member of our chosen basis from twelve to ten.

Given our focus on the original form  $\bar{\Omega}_{\mathcal{P}}$  in Eq. (3.3), we find that the forms  $\{\bar{\Omega}_{\mathcal{P}_i}\}$  in Eq. (3.6a) can be combined through the following linear superposition:

$$\bar{\Omega}_{\mathcal{P}} = \bar{\Omega}_{\mathcal{P}_1} + \bar{\Omega}_{\mathcal{P}_2} - \bar{\Omega}_{\mathcal{P}_3}, \quad (3.10)$$

which allows that we can select  $\mathcal{P}$  as an independent basis element, rather than relying on the three parent functions  $\{\mathcal{P}_i\}$ . Therefore, the ten independent members of our chosen basis belong to the following integral family:

$$\mathbf{I}_{\text{bub}} = (\mathcal{P}, \mathcal{F}_1, \mathcal{F}_2, \mathcal{F}_3, \tilde{\mathcal{F}}_1, \tilde{\mathcal{F}}_2, \tilde{\mathcal{F}}_3, Q_1, Q_2, Q_3)^T. \quad (3.11)$$

Indeed, the canonical forms associated with the bounded chambers naturally provide an “ $\varepsilon$ -form” [12, 13] basis for an integral family  $\mathbf{I}$ , where each integral has uniform transcendental

weight (UT). Hence,  $\mathbf{I}$  satisfies a linear system of differential equations in a simple canonical form, governed by a first-order equation:

$$d\mathbf{I}(\mathbf{z}, \varepsilon) = \varepsilon \tilde{A}(\mathbf{z})\mathbf{I}(\mathbf{z}, \varepsilon), \quad (3.12)$$

where  $\mathbf{z}$  is the set of all independent kinematic variables, for the two-site one-loop bubble case,  $\mathbf{z} = \{X_1, X_2, Y_1, Y_2\}$ . And the matrix  $\tilde{A}$  has the dlog form:

$$\tilde{A}(\mathbf{z}) = \sum_i c_i \text{dlog}[w_i(\mathbf{z})] \equiv \sum_i c_i l_i, \quad (3.13)$$

where the matrix  $\tilde{A}$  obeys the following integrability conditions:

$$d\tilde{A} = 0, \quad \tilde{A} \wedge \tilde{A} = 0. \quad (3.14)$$

Further, in the above expression (3.13),  $\{c_i\}$  are the constant matrices and  $\{w_i\}$  represent the “(symbol) letters” [19, 20] which are the rational or algebraic functions of kinematic variables, and the set of all letters are called the “alphabet”. For convenience, we have defined the dlog form of  $w_i$  as  $l_i$  in Eq. (3.13). In the subsequent discussions, we refer to  $l_i$  as a letter and the complete set of all independent  $l_i$  as the alphabet. In the following sections, we will analysis the structure of  $\tilde{A}$  arising in the bubble and the tadpole cases.

### 3.1.2 Derivation of Canonical DEs

In this section, we will calculate the canonical differential equations (3.12) by using the approach of integration-by-parts (IBP). We start by considering the first set of Eq. (3.5) i.e.,  $\mathbf{F}_1 = \{\mathcal{P}_1, \mathcal{F}_1, \tilde{\mathcal{F}}_1, \mathcal{Q}_1\}$ , where the total derivative for  $\mathbf{F}_1$  is given by

$$d\mathbf{F}_1 = \partial_{X_1}\mathbf{F}_1 dX_1 + \partial_{X_2}\mathbf{F}_1 dX_2 + \partial_{Y_1}\mathbf{F}_1 dY_1 + \partial_{Y_2}\mathbf{F}_1 dY_2. \quad (3.15)$$

For the parent function  $\mathcal{P}_1$  in  $\mathbf{F}_1$ , we observe that the differentiation of  $\mathcal{P}_1$  with respect to the external energy  $X_1$  is equal to the derivative with respect to  $x_1$ . Thus, we can compute

$$\begin{aligned} \partial_{X_1}\mathcal{P}_1 &= \int d\mu \partial_{x_1} \bar{\Omega}_{\mathcal{P}_1} = \varepsilon \int d\mu \left( -\frac{\bar{\Omega}_{\mathcal{P}_1}}{T_1} \right) \\ &= \varepsilon \int d\mu \left\{ \left( \text{Res} \left[ \frac{-\bar{\Omega}_{\mathcal{P}_1}}{T_1} \right]_{L_1=0}, \text{Res} \left[ \frac{-\bar{\Omega}_{\mathcal{P}_1}}{T_1} \right]_{L_2=0} \right) (\bar{\Omega}_{\mathcal{P}_1}, \bar{\Omega}_{\mathcal{F}_1})^T \right\} \\ &= \varepsilon \int d\mu \left[ \frac{1}{X_1+Y_1+Y_2} \bar{\Omega}_{\mathcal{P}_1} + \frac{2Y_2}{(X_1+Y_1-Y_2)(X_1+Y_1+Y_2)} \bar{\Omega}_{\mathcal{F}_1} \right] \\ &= \varepsilon \left[ \frac{1}{X_1+Y_1+Y_2} \mathcal{P}_1 + \left( \frac{1}{X_1+Y_1-Y_2} - \frac{1}{X_1+Y_1+Y_2} \right) \mathcal{F}_1 \right]. \end{aligned} \quad (3.16)$$

Similarly, the differentiation of  $\mathcal{P}_1$  with respect to  $X_2$  proceeds analogously to that of  $X_1$  and we simply need to replace  $X_1 \rightarrow X_2$  and  $\mathcal{F}_1 \rightarrow \tilde{\mathcal{F}}_1$  in Eq. (3.16) and obtain

$$\partial_{X_2}\mathcal{P}_1 = \varepsilon \left[ \frac{1}{X_2+Y_1+Y_2} \mathcal{P}_1 + \left( \frac{1}{X_2+Y_1-Y_2} - \frac{1}{X_2+Y_1+Y_2} \right) \tilde{\mathcal{F}}_1 \right]. \quad (3.17)$$

The calculation of differentiation of  $\mathcal{P}_1$  with respect to the internal energies  $Y_1$  and  $Y_2$  is non-trivial. However, these derivatives can be intuitively computed, yielding

$$\begin{aligned}\partial_{Y_1}\mathcal{P}_1 &= \int d\mu \left( \partial_{x_1} \bar{\Omega}_{\mathcal{P}_1} + \partial_{x_2} \bar{\Omega}_{\mathcal{P}_1} \right) \\ &= \varepsilon \left[ \left( \frac{1}{X_1+Y_1+Y_2} + \frac{1}{X_2+Y_1+Y_2} \right) \mathcal{P}_1 + \left( \frac{1}{X_1+Y_1-Y_2} - \frac{1}{X_1+Y_1+Y_2} \right) \mathcal{F}_1 \right. \\ &\quad \left. + \left( \frac{1}{X_2+Y_1-Y_2} - \frac{1}{X_2+Y_1+Y_2} \right) \tilde{\mathcal{F}}_1 \right],\end{aligned}\quad (3.18a)$$

$$\begin{aligned}\partial_{Y_2}\mathcal{P}_1 &= \int d\mu \left[ \partial_{x_1} \left( \frac{-x_1-X_1-Y_1}{Y_2} \bar{\Omega}_{\mathcal{P}_1} \right) + \partial_{x_2} \left( \frac{-x_2-X_2-Y_2}{Y_1} \bar{\Omega}_{\mathcal{P}_1} \right) \right] \\ &= \varepsilon \left[ \left( \frac{1}{X_1+Y_1+Y_2} + \frac{1}{X_2+Y_1+Y_2} \right) \mathcal{P}_1 - \left( \frac{1}{X_1+Y_1-Y_2} + \frac{1}{X_1+Y_1+Y_2} \right) \mathcal{F}_1 \right. \\ &\quad \left. - \left( \frac{1}{X_2+Y_1-Y_2} + \frac{1}{X_2+Y_1+Y_2} \right) \tilde{\mathcal{F}}_1 \right].\end{aligned}\quad (3.18b)$$

In terms of total derivative (3.19) and expressing in dlog forms, we finally obtain the canonical differential equation for  $\mathcal{P}_1$  as follows:

$$\begin{aligned}d\mathcal{P}_1 &= \varepsilon \left[ (\mathcal{P}_1 - \mathcal{F}_1) d\log(X_1+Y_1+Y_2) + (\mathcal{P}_1 - \tilde{\mathcal{F}}_1) d\log(X_2+Y_1+Y_2) \right. \\ &\quad \left. + \mathcal{F}_1 d\log(X_1+Y_1-Y_2) + \tilde{\mathcal{F}}_1 d\log(X_2+Y_1-Y_2) \right].\end{aligned}\quad (3.19)$$

Next, we examine the differentiation of the decedent functions  $\mathcal{F}_1, \tilde{\mathcal{F}}_1$  and  $\mathcal{Q}_1$ . For  $\mathcal{F}_1$ , the differential results with respect to external energies are computed as:

$$\begin{aligned}\partial_{X_1}\mathcal{F}_1 &= \int d\mu \left[ \partial_{x_1} \left( \frac{-T_1}{X_1+Y_1-Y_2} \bar{\Omega}_{\mathcal{F}_1} \right) + \partial_{x_2} \left( \frac{-L_2}{X_1+Y_1-Y_2} \bar{\Omega}_{\mathcal{F}_1} \right) \right] \\ &= \varepsilon \int d\mu \left\{ \left( \text{Res} \left[ \frac{\bar{\Omega}_{\mathcal{F}_1}}{X_1+Y_1-Y_2} \right]_{\substack{T_1=0 \\ L_2=0}}, \text{Res} \left[ \frac{\bar{\Omega}_{\mathcal{F}_1}}{X_1+Y_1-Y_2} \right]_{\substack{T_1=0 \\ T_2=0}} \right) (\bar{\Omega}_{\mathcal{F}_1}, \bar{\Omega}_{\mathcal{Q}_1})^T \right. \\ &\quad \left. + \left( \text{Res} \left[ \frac{L_2 \bar{\Omega}_{\mathcal{F}_1}}{T_2(X_1+Y_1-Y_2)} \right]_{\substack{T_1=0 \\ L_2=0}}, \text{Res} \left[ \frac{L_2 \bar{\Omega}_{\mathcal{F}_1}}{T_2(X_1+Y_1-Y_2)} \right]_{\substack{T_1=0 \\ T_2=0}} \right) (\bar{\Omega}_{\mathcal{F}_1}, \bar{\Omega}_{\mathcal{Q}_1})^T \right\} \\ &= \varepsilon \left[ \frac{1}{X_1+Y_1-Y_2} \mathcal{F}_1 + \frac{1}{X_1+X_2+2Y_1} \mathcal{Q}_1 \right],\end{aligned}\quad (3.20a)$$

$$\begin{aligned}\partial_{X_2}\mathcal{F}_1 &= \int d\mu \partial_{x_2} \bar{\Omega}_{\mathcal{F}_1} \\ &= \varepsilon \left[ \frac{1}{X_2+Y_1+Y_2} \mathcal{F}_1 + \left( \frac{1}{X_1+X_2+2Y_1} - \frac{1}{X_2+Y_1+Y_2} \right) \mathcal{Q}_1 \right],\end{aligned}\quad (3.20b)$$

and the results for differentiation with respect to the internal energies are

$$\begin{aligned}\partial_{Y_1}\mathcal{F}_1 &= \int d\mu \left[ \partial_{x_1} \left( \frac{-T_1}{X_1+Y_1-Y_2} \bar{\Omega}_{\mathcal{F}_1} \right) + \partial_{x_2} \left( \frac{-T_1-2L_2+D_1}{X_1+Y_1-Y_2} \bar{\Omega}_{\mathcal{F}_1} \right) \right] \\ &= \varepsilon \left[ \left( \frac{1}{X_1+Y_1-Y_2} + \frac{1}{X_2+Y_1+Y_2} \right) \mathcal{F}_1 + \left( \frac{2}{X_1+X_2+2Y_1} - \frac{1}{X_2+Y_1+Y_2} \right) \mathcal{Q}_1 \right],\end{aligned}\quad (3.21a)$$

$$\partial_{Y_2}\mathcal{F}_1 = \int d\mu \left[ \partial_{x_1} \left( \frac{T_1}{X_1+Y_1-Y_2} \bar{\Omega}_{\mathcal{F}_1} \right) + \partial_{x_2} \left( \frac{-T_1+D_1}{X_1+Y_1-Y_2} \bar{\Omega}_{\mathcal{F}_1} \right) \right]$$

$$= \varepsilon \left[ \left( -\frac{1}{X_1+Y_1-Y_2} + \frac{1}{X_2+Y_1+Y_2} \right) \mathcal{F}_1 - \frac{1}{X_2+Y_1+Y_2} \mathcal{Q}_1 \right]. \quad (3.21b)$$

The calculation for  $\tilde{\mathcal{F}}_1$  is similar to that of  $\mathcal{F}_1$ , we will not provide the details. Hence, in terms of the total derivative, we can obtain the differential equations for  $\mathcal{F}_1$  and  $\tilde{\mathcal{F}}_1$ :

$$\begin{aligned} d\mathcal{F}_1 = \varepsilon [ & \mathcal{F}_1 d\log(X_1+Y_1-Y_2) + (\mathcal{F}_1 - \mathcal{Q}_1) d\log(X_2+Y_1+Y_2) \\ & + \mathcal{Q}_1 d\log(X_1+X_2+2Y_1) ], \end{aligned} \quad (3.22a)$$

$$\begin{aligned} d\tilde{\mathcal{F}}_1 = \varepsilon [ & \tilde{\mathcal{F}}_1 d\log(X_2+Y_1-Y_2) + (\tilde{\mathcal{F}}_1 - \mathcal{Q}_1) d\log(X_1+Y_1+Y_2) \\ & + \mathcal{Q}_1 d\log(X_1+X_2+2Y_1) ]. \end{aligned} \quad (3.22b)$$

Finally, for the function  $\mathcal{Q}_1$ , we can derive

$$\begin{aligned} \partial_{X_1} \mathcal{Q}_1 &= \int d\mu \left[ \partial_{x_1} \left( \frac{-T_1}{X_1+X_2+2Y_1} \bar{\Omega}_{\mathcal{Q}_1} \right) + \partial_{x_2} \left( \frac{-T_2}{X_1+X_2+2Y_1} \bar{\Omega}_{\mathcal{Q}_1} \right) \right] \\ &= 2\varepsilon \int d\mu \left( \text{Res} \left[ \frac{\bar{\Omega}_{\mathcal{Q}_1}}{X_1+X_2+2Y_1} \right]_{\substack{T_1=0 \\ T_2=0}} \bar{\Omega}_{\mathcal{Q}_1} \right) = 2\varepsilon \left( \frac{1}{X_1+X_2+2Y_1} \right) \mathcal{Q}_1, \end{aligned} \quad (3.23a)$$

$$\partial_{X_2} \mathcal{Q}_1 = \partial_{X_1} \mathcal{Q}_1 = 2\varepsilon \left( \frac{1}{X_1+X_2+2Y_1} \right) \mathcal{Q}_1, \quad (3.23b)$$

$$\begin{aligned} \partial_{Y_1} \mathcal{Q}_1 &= \int d\mu \left[ \partial_{x_1} \left( \frac{-2T_1}{X_1+X_2+2Y_1} \bar{\Omega}_{\mathcal{Q}_1} \right) + \partial_{x_2} \left( \frac{-2T_2}{X_1+X_2+2Y_1} \bar{\Omega}_{\mathcal{Q}_1} \right) \right] \\ &= \frac{4\varepsilon}{X_1+X_2+2Y_1} \mathcal{Q}_1, \end{aligned} \quad (3.23c)$$

$$\partial_{Y_2} \mathcal{Q}_1 = 0. \quad (3.23d)$$

Therefore, the differential equation for  $\mathcal{Q}_1$  is given by

$$d\mathcal{Q}_1 = 2\varepsilon \mathcal{Q}_1 d\log(X_1+X_2+2Y_1). \quad (3.24)$$

The canonical differential equations for  $\mathbf{F}_2$  can be directly derived from those of  $\mathbf{F}_1$  by substituting  $Y_1 \rightarrow Y_2$  in the dlog forms and relabeling the function subscripts  $1 \rightarrow 2$ . The resulting equations are summarized as follows:

$$\begin{aligned} d\mathcal{P}_2 = \varepsilon [ & (\mathcal{P}_2 - \mathcal{F}_2) d\log(X_1+Y_1+Y_2) + (\mathcal{P}_2 - \tilde{\mathcal{F}}_2) d\log(X_2+Y_1+Y_2) \\ & + \mathcal{F}_2 d\log(X_1-Y_1+Y_2) + \tilde{\mathcal{F}}_2 d\log(X_2-Y_1+Y_2) ], \end{aligned} \quad (3.25a)$$

$$\begin{aligned} d\mathcal{F}_2 = \varepsilon [ & \mathcal{F}_2 d\log(X_1-Y_1+Y_2) + (\mathcal{F}_2 - \mathcal{Q}_2) d\log(X_2+Y_1+Y_2) \\ & + \mathcal{Q}_2 d\log(X_1+X_2+2Y_2) ], \end{aligned} \quad (3.25b)$$

$$\begin{aligned} d\tilde{\mathcal{F}}_2 = \varepsilon [ & \tilde{\mathcal{F}}_2 d\log(X_2-Y_1+Y_2) + (\tilde{\mathcal{F}}_2 - \mathcal{Q}_2) d\log(X_1+Y_1+Y_2) \\ & + \mathcal{Q}_2 d\log(X_2+X_2+2Y_2) ], \end{aligned} \quad (3.25c)$$

$$d\mathcal{Q}_2 = 2\varepsilon \mathcal{Q}_2 d\log(X_1+X_2+2Y_2). \quad (3.25d)$$

In Appendix A.1, we provide the detailed derivation of the canonical differential equations for  $\mathbf{F}_3$ . Here, we only summarize the results as follows:

$$d\mathcal{P}_3 = \varepsilon [ (\mathcal{P}_3 - \mathcal{F}_3) d\log(X_1+Y_1+Y_2) + (\mathcal{P}_3 - \tilde{\mathcal{F}}_3) d\log(X_2+Y_1+Y_2) ]$$

$$+ \mathcal{F}_3 \text{dlog}(X_1 - Y_1 - Y_2) + \tilde{\mathcal{F}}_3 \text{dlog}(X_2 - Y_1 - Y_2) \Big], \quad (3.26a)$$

$$d\mathcal{F}_3 = \varepsilon [\mathcal{F}_3 \text{dlog}(X_1 - Y_1 - Y_2) + (\mathcal{F}_3 - \mathcal{Q}_3) \text{dlog}(X_2 + Y_1 + Y_2) + \mathcal{Q}_3 \text{dlog}(X_1 + X_2)], \quad (3.26b)$$

$$d\tilde{\mathcal{F}}_3 = \varepsilon [\tilde{\mathcal{F}}_3 \text{dlog}(X_2 - Y_1 - Y_2) + (\tilde{\mathcal{F}}_3 - \mathcal{Q}_3) \text{dlog}(X_1 + Y_1 + Y_2) + \mathcal{Q}_3 \text{dlog}(X_1 + X_2)], \quad (3.26c)$$

$$d\mathcal{Q}_3 = 2\varepsilon \mathcal{Q}_3 \text{dlog}(X_1 + X_2). \quad (3.26d)$$

In addition, based on Eq. (3.10), we combine Eq. (3.19), Eq. (3.25a) with Eq. (3.26a) to derive the final differential equation for  $\mathcal{P}$ :

$$\begin{aligned} d\mathcal{P} = \varepsilon \Big[ & \left( \mathcal{P} - \sum_{i=1}^3 \mathcal{F}_i \right) \text{dlog}(X_1 + Y_1 + Y_2) + \left( \mathcal{P} - \sum_{j=1}^3 \tilde{\mathcal{F}}_j \right) \text{dlog}(X_2 + Y_1 + Y_2) \\ & + \mathcal{F}_1 \text{dlog}(X_1 + Y_1 - Y_2) + \tilde{\mathcal{F}}_1 \text{dlog}(X_2 + Y_1 - Y_2) + \mathcal{F}_2 \text{dlog}(X_1 - Y_1 + Y_2) \\ & + \tilde{\mathcal{F}}_2 \text{dlog}(X_2 - Y_1 + Y_2) + \mathcal{F}_3 \text{dlog}(X_1 - Y_1 - Y_2) + \tilde{\mathcal{F}}_3 \text{dlog}(X_2 - Y_1 - Y_2) \Big], \quad (3.27) \end{aligned}$$

where we have rescaled  $\mathcal{F}_3 \rightarrow -\mathcal{F}_3$ ,  $\tilde{\mathcal{F}}_3 \rightarrow -\tilde{\mathcal{F}}_3$  and  $\mathcal{Q}_3 \rightarrow -\mathcal{Q}_3$ . These rescaling are permissible due to the homogeneous nature of the system of canonical differential equation, which is invariant under sign changes of the components.

Then, by systematically compiling and analyzing all the canonical differential equations derived above, we have carefully organized the findings to ensure clarity and consistency. The results are summarized as follows:

$$\begin{aligned} d\mathcal{P} = \varepsilon [ & \mathcal{P}(l_1 + l_2) + \mathcal{F}_1(l_3 - l_1) + \tilde{\mathcal{F}}_1(l_4 - l_2) + \mathcal{F}_2(l_5 - l_1) + \tilde{\mathcal{F}}_2(l_6 - l_2) \\ & + \mathcal{F}_3(l_7 - l_1) + \tilde{\mathcal{F}}_3(l_8 - l_2) ], \\ d\mathcal{F}_1 = \varepsilon [ & \mathcal{F}_1(l_2 + l_3) + \mathcal{Q}_1(l_9 - l_2) ], & d\tilde{\mathcal{F}}_1 = \varepsilon [ \tilde{\mathcal{F}}_1(l_1 + l_4) + \mathcal{Q}_1(l_9 - l_1) ], \\ d\mathcal{F}_2 = \varepsilon [ & \mathcal{F}_2(l_2 + l_5) + \mathcal{Q}_2(l_{10} - l_2) ], & d\tilde{\mathcal{F}}_2 = \varepsilon [ \tilde{\mathcal{F}}_2(l_1 + l_6) + \mathcal{Q}_2(l_{10} - l_1) ], \\ d\mathcal{F}_3 = \varepsilon [ & \mathcal{F}_3(l_2 + l_7) + \mathcal{Q}_3(l_{11} - l_2) ], & d\tilde{\mathcal{F}}_3 = \varepsilon [ \tilde{\mathcal{F}}_3(l_1 + l_8) + \mathcal{Q}_3(l_{11} - l_1) ], \\ d\mathcal{Q}_1 = 2\varepsilon \mathcal{Q}_1 l_9, & \quad d\mathcal{Q}_2 = 2\varepsilon \mathcal{Q}_2 l_{10}, \quad d\mathcal{Q}_3 = 2\varepsilon \mathcal{Q}_3 l_{11}. \quad (3.28) \end{aligned}$$

Here, in the expressions of Eq. (3.28), the letters are defined as:  $l_i = \text{dlog}(w_i)$  with  $i = 1, \dots, 11$ , and the explicit forms of the letters are given by

$$\begin{aligned} l_1 &= \text{dlog}(X_1 + Y_1 + Y_2), & l_2 &= \text{dlog}(X_2 + Y_1 + Y_2), & l_3 &= \text{dlog}(X_1 + Y_1 - Y_2), \\ l_4 &= \text{dlog}(X_2 + Y_1 - Y_2), & l_5 &= \text{dlog}(X_1 - Y_1 + Y_2), & l_6 &= \text{dlog}(X_2 - Y_1 + Y_2), \\ l_7 &= \text{dlog}(X_1 - Y_1 - Y_2), & l_8 &= \text{dlog}(X_2 - Y_1 - Y_2), & l_9 &= \text{dlog}(X_1 + X_2 + 2Y_1), \\ l_{10} &= \text{dlog}(X_1 + X_2 + 2Y_2), & l_{11} &= \text{dlog}(X_1 + X_2). \quad (3.29) \end{aligned}$$

The solution to Eq. (3.28) is analogous to that for tree-level cases [7] and can be summarized as follows: (i). Solve the homologous equations for  $\mathcal{Q}_i$ . (ii). Substitute the solutions of  $\mathcal{Q}_i$  into the equations for  $\mathcal{F}_i, \tilde{\mathcal{F}}_i$  to determine  $\mathcal{F}_i, \tilde{\mathcal{F}}_i$ . (iii). Define a equation  $d\mathcal{P}_{\text{hom}} \equiv d\mathcal{P} -$

$\sum_{i=1}^3 (d\mathcal{F}_i + d\tilde{\mathcal{F}}_i - d\mathcal{Q}_i)$  which is in homogeneous nature and solve for  $\mathcal{P}_{\text{hom}}$ . (iv). Substitute the results for  $\mathcal{F}_i$ ,  $\tilde{\mathcal{F}}_i$  and  $\mathcal{Q}_i$  back into  $\mathcal{P}_{\text{hom}}$  to obtain the complete solution for  $\mathcal{P}_{\text{hom}}$ .

Next, we examine the structure of the matrix  $\tilde{A}$  as presented in Eq. (3.12). Referring to Eq. (3.28), the matrix  $\tilde{A}$  of the current bubble system is explicitly given by

$$\tilde{A}_{\text{bub}} = \begin{pmatrix} l_1+l_2 & l_3-l_1 & l_5-l_1 & l_7-l_1 & l_4-l_2 & l_6-l_2 & l_8-l_2 & 0 & 0 & 0 \\ 0 & l_2+l_3 & 0 & 0 & 0 & 0 & 0 & l_9-l_2 & 0 & 0 \\ 0 & 0 & l_2+l_5 & 0 & 0 & 0 & 0 & 0 & l_{10}-l_2 & 0 \\ 0 & 0 & 0 & l_2+l_7 & 0 & 0 & 0 & 0 & 0 & l_{11}-l_2 \\ 0 & 0 & 0 & 0 & l_1+l_4 & 0 & 0 & l_9-l_1 & 0 & 0 \\ 0 & 0 & 0 & 0 & 0 & l_1+l_6 & 0 & 0 & l_{10}-l_1 & 0 \\ 0 & 0 & 0 & 0 & 0 & 0 & l_1+l_8 & 0 & 0 & l_{11}-l_1 \\ 0 & 0 & 0 & 0 & 0 & 0 & 0 & 2l_9 & 0 & 0 \\ 0 & 0 & 0 & 0 & 0 & 0 & 0 & 0 & 2l_{10} & 0 \\ 0 & 0 & 0 & 0 & 0 & 0 & 0 & 0 & 0 & 2l_{11} \end{pmatrix}, \quad (3.30)$$

where a careful verification confirms that  $\tilde{A}_{\text{bub}}$  satisfies the integrability conditions outlined in Eq. (3.14), ensuring consistency within the underlying theoretical framework.

An intriguing aspect of our analysis involves performing a finite sequence of elementary transformations on the matrix (3.30). And these transformations yield the following matrix as follows:

$$\tilde{A}'_{\text{bub}} = \begin{pmatrix} 2l_{11} & 0 & 0 & 0 & 0 & 0 & 0 & 0 & 0 & 0 \\ 0 & 2l_9 & 0 & 0 & 0 & 0 & 0 & 0 & 0 & 0 \\ 0 & 0 & 2l_{10} & 0 & 0 & 0 & 0 & 0 & 0 & 0 \\ l_1-l_8 & 0 & 0 & l_8+l_1 & 0 & 0 & 0 & 0 & 0 & 0 \\ l_7-l_2 & 0 & 0 & 0 & l_2+l_7 & 0 & 0 & 0 & 0 & 0 \\ 0 & 0 & 0 & 0 & 0 & l_1+l_2 & 0 & 0 & 0 & 0 \\ 0 & l_4-l_1 & 0 & 0 & 0 & 0 & l_1+l_4 & 0 & 0 & 0 \\ 0 & 0 & l_6-l_1 & 0 & 0 & 0 & 0 & l_1+l_6 & 0 & 0 \\ 0 & l_2-l_3 & 0 & 0 & 0 & 0 & 0 & 0 & l_2+l_3 & 0 \\ 0 & 0 & l_2-l_5 & 0 & 0 & 0 & 0 & 0 & 0 & l_2+l_5 \end{pmatrix}. \quad (3.31)$$

This matches perfectly with the matrix derived using the dual twisted cohomology method presented in Ref. [5]. Thus, for the first time, we have reproduced the two-site one-loop result using the method of cohomology. This agreement provides additional confidence in our methods and highlights the robustness of our findings in relation to established theoretical frameworks.

Furthermore, we can demonstrate that in the limit  $\varepsilon \rightarrow 0$ , the equations derived in FRW cosmology will reduce to the equations in dS spacetime. By imposing the following rescale in Eq. (3.28)

$$\mathcal{F}_i \rightarrow \mathcal{F}_i/\varepsilon, \quad \tilde{\mathcal{F}}_i \rightarrow \tilde{\mathcal{F}}_i/\varepsilon, \quad \mathcal{Q}_i \rightarrow \mathcal{Q}_i/\varepsilon^2, \quad (3.32)$$

and taking the limit  $\varepsilon \rightarrow 0$ , we can obtain

$$\begin{aligned} d\mathcal{P} &= \mathcal{F}_1(l_3-l_1) + \tilde{\mathcal{F}}_1(l_4-l_2) + \mathcal{F}_2(l_5-l_1) + \tilde{\mathcal{F}}_2(l_6-l_2) + \mathcal{F}_3(l_7-l_1) + \tilde{\mathcal{F}}_3(l_8-l_2), \\ d\mathcal{F}_1 &= \mathcal{Q}_1(l_9-l_2), \quad d\tilde{\mathcal{F}}_1 = \mathcal{Q}_1(l_9-l_1), \quad d\mathcal{F}_2 = \mathcal{Q}_2(l_{10}-l_2), \quad d\tilde{\mathcal{F}}_2 = \mathcal{Q}_2(l_{10}-l_1), \\ d\mathcal{F}_3 &= \mathcal{Q}_3(l_{11}-l_2), \quad d\tilde{\mathcal{F}}_3 = \mathcal{Q}_3(l_{11}-l_1), \quad d\mathcal{Q}_1 = d\mathcal{Q}_2 = d\mathcal{Q}_3 = 0, \end{aligned} \quad (3.33)$$

where it is not difficult to check the matrix  $\tilde{A}_{\text{bub}}^{\text{dS}}$  obeys the integrability conditions (3.14). Subsequently, based on the differential equations (3.33), we can derive the symbol for two-site one-loop bubble correlator:

$$\begin{aligned} \mathcal{S}_{(2,1)}^{\text{bub}} &= (w_9/w_2) \otimes (w_3/w_1) + (w_9/w_1) \otimes (w_4/w_2) \\ &\quad + (w_{10}/w_2) \otimes (w_5/w_1) + (w_{10}/w_1) \otimes (w_6/w_2) \\ &\quad + (w_{11}/w_2) \otimes (w_7/w_1) + (w_{11}/w_1) \otimes (w_8/w_2), \end{aligned} \quad (3.34)$$

where we revert the previously rescaled  $\mathcal{F}_3$ ,  $\tilde{\mathcal{F}}_3$  and  $\mathcal{Q}_3$  back to their original forms. Further, by using the package of *PolyLogTools* [21], we can derive the transcendental function with transcendental degree-2 after integrating the symbol (3.34),

$$\begin{aligned} f_{(2,1)}^{\text{bub}} &= -\pi^2/6 + \text{Li}_2(w_3/w_9) + \text{Li}_2(w_4/w_9) + \text{Li}_1(w_3/w_9)\text{Li}_1(w_4/w_9) \\ &\quad + \text{Li}_2(w_5/w_{10}) + \text{Li}_2(w_6/w_{10}) + \text{Li}_1(w_5/w_{10})\text{Li}_1(w_6/w_{10}) \\ &\quad - \text{Li}_2(w_7/w_{11}) - \text{Li}_2(w_8/w_{11}) - \text{Li}_1(w_7/w_{11})\text{Li}_1(w_8/w_{11}). \end{aligned} \quad (3.35)$$

Both  $\mathcal{S}_{(2,1)}^{\text{bub}}$  and  $f_{(2,1)}^{\text{bub}}$  are consistent with the results presented in Ref. [22]. This alignment reinforces the correctness of our method and demonstrates that our approach accurately captures the underlying physical relationships, contributing to a reliable interpretation of the two-site one-loop graph in de Sitter spacetime.

### 3.2 Two-Site One-Loop Tadpole

At two-site one-loop, another topology is the tadpole contribution which is shown in Fig. 3. The wavefunction coefficient for a tadpole graph, when approached from the perspective of positive geometry [18], corresponds to a cosmological polytope with the structure of a square pyramid, which can be effectively triangulated and divided into two distinct zero-edge-weight smaller polytopes [3]. The pole structures of these smaller polytopes notably align with those of tree-level diagrams, allowing the application of methodologies from

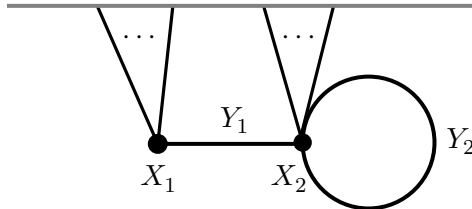


**Figure 3.** The Feynman diagram for the two-site one-loop tadpole-type wavefunction coefficient.



Refs. [7, 8] to derive the associated differential equations for analyzing the system. Further detailed elaboration on this computation method is not included here.

We start by computing the wavefunction coefficient for two-site one-loop tadpole graph in flat spacetime:

$$\begin{aligned}\tilde{\psi}_{(2,1)}^{\text{tad}} &= i^2 \int_{-\infty}^0 d\eta_1 \int_{-\infty}^0 d\eta_2 K_1(X_1; \eta_1) K_2(X_2; \eta_2) G_1(Y_1; \eta_1, \eta_2) G_2(Y_2; \eta_2, \eta_2) \\ &= \frac{X_1 + Y_1 + 2(X_2 + Y_2)}{(X_1 + X_2)(X_1 + Y_1)(X_2 + Y_1)(X_1 + X_2 + 2Y_2)(X_2 + Y_1 + 2Y_2)}.\end{aligned}\quad (3.36)$$

Similarly, the FRW wavefunction coefficient for tadpole can be obtained by imposing the energy shifts:  $(X_1, X_2) \rightarrow (X_1 + x_1, X_2 + x_2)$  on its flat-space form. After incorporating the twister and normalization factors, we have

$$\begin{aligned}\psi_{(2,1)}^{\text{tad}} &= 4Y_1 Y_2 \int dx_1 \wedge dx_2 (x_1 x_2)^\varepsilon \tilde{\psi}_{(2,1)}^{\text{tad}} \Big|_{X_2 \rightarrow X_2 + x_2}^{X_1 \rightarrow X_1 + x_1} \\ &= -2Y_1 \int dx_1 \wedge dx_2 (T_1 T_2)^\varepsilon \left( \frac{1}{L_1 \bar{L}_2 D_2} - \frac{1}{L_1 L_2 D_3} \right) \\ &\equiv \int d\mu \bar{\Omega}_{\mathcal{P}_{\text{tad}}},\end{aligned}\quad (3.37)$$

where the hyperplanes are defined as follows:

$$\begin{aligned}T_1 &= x_1, & T_2 &= x_2, \\ L_1 &= x_1 + X_1 + Y_1, & L_2 &= x_2 + X_2 + Y_1, & \bar{L}_2 &= L_2 + 2Y_2, \\ D_2 &= x_1 + x_2 + X_1 + X_2 + 2Y_2, & D_3 &= x_1 + x_2 + X_1 + X_2.\end{aligned}\quad (3.38)$$

### 3.2.1 Hyperplane Arrangements and Derivation of Canonical DEs

Similar to the analysis of bubble diagram, in Eq. (3.38), those hyperplanes can be arranged in  $(x_1, x_2)$ -plane as illustrated in Fig. 4. In this factorization, one term is exactly tree function and the other is a shifted tree with  $X_2 \rightarrow X_2 + 2Y_2$ . This observation enable us to immediately read out the differential equations obeyed by the tadpole system, which is nothing but a linear combination of the two tree-level systems. Therefore, the total integral family  $\mathbf{I}_{\text{tad}}$  contains eight independent members which can be divided into two sets:  $\mathbf{F}_2 = \{\mathcal{P}_2, \mathcal{F}_2, \tilde{\mathcal{F}}_2, \mathcal{Q}_2\}$  and  $\mathbf{F}_3 = \{\mathcal{P}_3, \mathcal{F}_3, \tilde{\mathcal{F}}_3, \mathcal{Q}_3\}$ . The associated canonical forms for  $\mathbf{F}_2$  and  $\mathbf{F}_3$  are defined in the similar way of Eq. (3.7):

$$\text{Layer-0: } \quad \bar{\Omega}_{\mathcal{P}_2} = \frac{-2Y_1}{L_1 \bar{L}_2 D_2}, \quad \bar{\Omega}_{\mathcal{P}_3} = \frac{-2Y_1}{L_1 L_2 D_3}, \quad (3.39a)$$

$$\text{Layer-1: } \quad \bar{\Omega}_{\mathcal{F}_2} = \frac{X_1 - Y_1}{T_1 \bar{L}_2 D_2}, \quad \bar{\Omega}_{\mathcal{F}_3} = \frac{X_1 - Y_1}{T_1 L_2 D_3}, \quad (3.39b)$$

$$\bar{\Omega}_{\tilde{\mathcal{F}}_2} = \frac{X_2 - Y_1 + 2Y_2}{T_2 L_1 D_2}, \quad \bar{\Omega}_{\tilde{\mathcal{F}}_3} = \frac{X_2 - Y_1}{T_2 L_1 D_3}, \quad (3.39c)$$

$$\text{Layer-2: } \quad \bar{\Omega}_{\mathcal{Q}_2} = \frac{X_1 + X_2 + 2Y_2}{T_1 T_2 D_2}, \quad \bar{\Omega}_{\mathcal{Q}_3} = \frac{X_1 + X_2}{T_1 T_2 D_3}. \quad (3.39d)$$

Notably, unlike the bubble case, the  $D_1$ -plane in the hyperplane arrangement (cf. Fig. 3) transforms into the hyperplane  $\bar{L}_2$  which is parallel to hyperplanes  $T_2$  and  $L_2$  in the tadpole configuration (cf. Fig. 4). This transformation eliminates the presence of  $\mathbf{F}_1$  in the bubble case. Meanwhile, the definitions of canonical forms for  $\mathbf{F}_2$  and  $\mathbf{F}_3$  in Eq. (3.39) remain similar to those in bubble case (3.7), albeit with some slight modifications to the definition of hyperplanes [cf. Eq. (3.38)]. Furthermore, there is another key difference from the bubble case. Although the differential forms  $\bar{\Omega}_{\mathcal{P}_{\text{tad}}}$ ,  $\bar{\Omega}_{\mathcal{P}_2}$  and  $\bar{\Omega}_{\mathcal{P}_3}$  obey the following linear relation  $\bar{\Omega}_{\mathcal{P}_{\text{tad}}} = \bar{\Omega}_{\mathcal{P}_2} - \bar{\Omega}_{\mathcal{P}_3}$ , it is not possible to combine the differential equations for  $\mathcal{P}_2$  and  $\mathcal{P}_3$  into a single equation for  $\mathcal{P}_{\text{tad}}$ . This is because  $\bar{\Omega}_{\mathcal{P}_2}$  and  $\bar{\Omega}_{\mathcal{P}_3}$  are associated with different  $L$ -pairs, which result in distinct letters. A more detailed discussion of this point will be provided in Section 3.2.2. Therefore, when selecting the integral family  $\mathbf{I}_{\text{tad}}$ , we treat  $\mathcal{P}_2$  and  $\mathcal{P}_3$  as two independent elements.

Then, using the IBP method presented in Section 3.2.1, it is straightforward to derive all the canonical differential equations associated with Eq. (3.39). The derived results are summarized below:

$$\begin{aligned}
d\mathcal{P}_2 &= \varepsilon [\mathcal{P}_2(l_1 + \bar{l}_2) + \mathcal{F}_2(l_3 - l_1) + \tilde{\mathcal{F}}_2(\bar{l}_4 - \bar{l}_2)], \\
d\mathcal{P}_3 &= \varepsilon [\mathcal{P}_3(l_1 + l_2) + \mathcal{F}_3(l_3 - l_1) + \tilde{\mathcal{F}}_3(l_4 - l_2)], \\
d\mathcal{F}_2 &= \varepsilon [\mathcal{F}_2(\bar{l}_2 + l_3) + \mathcal{Q}_2(\bar{l}_5 - \bar{l}_2)], & d\tilde{\mathcal{F}}_2 &= \varepsilon [\tilde{\mathcal{F}}_2(l_1 + \bar{l}_4) + \mathcal{Q}_2(\bar{l}_5 - l_1)], \\
d\mathcal{F}_3 &= \varepsilon [\mathcal{F}_3(l_2 + l_3) + \mathcal{Q}_3(l_5 - l_2)], & d\tilde{\mathcal{F}}_3 &= \varepsilon [\tilde{\mathcal{F}}_3(l_1 + l_4) + \mathcal{Q}_3(l_5 - l_1)], \\
d\mathcal{Q}_2 &= 2\varepsilon \mathcal{Q}_1 \bar{l}_5, & d\mathcal{Q}_3 &= 2\varepsilon \mathcal{Q}_2 l_5,
\end{aligned} \tag{3.40}$$

where the letters  $l_i = \text{dlog}(w_i)$  and  $\bar{l}_i = \text{dlog}(\bar{w}_i)$ , which are given by

$$l_1 = \text{dlog}(X_1 + Y_1), \quad l_2 = \text{dlog}(X_2 + Y_1), \quad \bar{l}_2 = \text{dlog}(X_2 + Y_1 + 2Y_2),$$

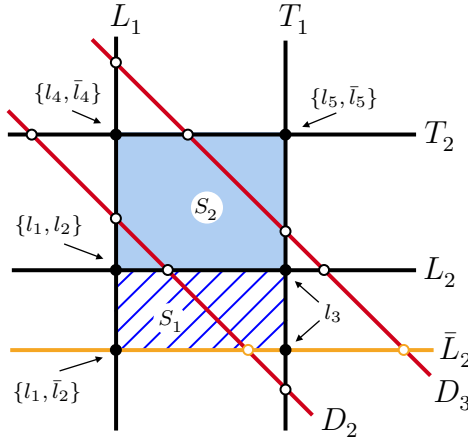


**Figure 4.** The complete hyperplane arrangement for two-site one-loop tadpole-type wavefunction coefficient. All the black and white intersection points represent the codimension-2 boundaries. Among these, the four intersection points of  $L_1 \cap L_2$ ,  $L_1 \cap \bar{L}_2$ ,  $L_1 \cap T_2$ ,  $L_2 \cap T_1$ ,  $\bar{L}_2 \cap T_1$  and  $T_1 \cap T_2$  are used to calculate the letters  $\{l_i\}$  in our chosen basis.

$$\begin{aligned}
l_3 &= \text{dlog}(X_1 - Y_1), & l_4 &= \text{dlog}(X_2 - Y_1), & \bar{l}_4 &= \text{dlog}(X_2 - Y_1 + 2Y_2), \\
l_5 &= \text{dlog}(X_1 + X_2), & \bar{l}_5 &= \text{dlog}(X_1 + X_2 + 2Y_2).
\end{aligned} \tag{3.41}$$

Similarly, by taking the dS limit  $\varepsilon \rightarrow 0$ , canonical differential equations (3.40) will reduce to the following forms:

$$\begin{aligned}
d\mathcal{P}_2 &= \mathcal{F}_2(l_3 - l_1) + \tilde{\mathcal{F}}_2(\bar{l}_4 - \bar{l}_2), & d\mathcal{P}_3 &= \mathcal{F}_3(l_3 - l_1) + \tilde{\mathcal{F}}_3(l_4 - l_2), \\
d\mathcal{F}_2 &= \mathcal{Q}_2(\bar{l}_5 - \bar{l}_2), & d\mathcal{F}_3 &= \mathcal{Q}_3(l_5 - l_2), \\
d\tilde{\mathcal{F}}_2 &= \mathcal{Q}_2(\bar{l}_5 - l_1), & d\tilde{\mathcal{F}}_3 &= \mathcal{Q}_3(l_5 - l_1), \\
d\mathcal{Q}_2 &= 0, & d\mathcal{Q}_3 &= 0,
\end{aligned} \tag{3.42}$$

where we can write down the symbol results:

$$\begin{aligned}
\mathcal{S}_{(2,1)}^{\text{tad}} &= (\bar{w}_5/\bar{w}_2) \otimes (w_3/w_1) + (\bar{w}_5/w_1) \otimes (\bar{w}_4/\bar{w}_2) \\
&\quad + (w_5/w_2) \otimes (w_3/w_1) + (w_5/w_1) \otimes (w_4/w_2),
\end{aligned} \tag{3.43}$$

and the transcendental function after integrating the symbol (3.43)

$$\begin{aligned}
f_{(2,1)}^{\text{tad}} &= -\pi^2/6 + \text{Li}_2(w_3/\bar{w}_5) + \text{Li}_2(\bar{w}_4/\bar{w}_5) + \text{Li}_1(\bar{w}_3/\bar{w}_5)\text{Li}_1(\bar{w}_4/\bar{w}_5) \\
&\quad + \text{Li}_2(w_3/w_5) + \text{Li}_2(w_4/w_5) + \text{Li}_1(w_3/w_5)\text{Li}_1(w_4/w_5),
\end{aligned} \tag{3.44}$$

where  $l_i = \text{dlog}(w_i)$  and  $\bar{l}_i = \text{dlog}(\bar{w}_i)$ .

### 3.2.2 New Features from Tadpole System and Triangle Basis

A closer look at the tadpole differential system (3.40) reveals distinct features against the bubble system as discussed in Section 3.1. Importantly, unlike the bubble case, the two parent functions  $\mathcal{P}_2$  and  $\mathcal{P}_3$  in tadpole system cannot be merged into a single function  $\mathcal{P}$  without comprising the uniform transcendental property. This distinction arises because the calculation of the differential equations for  $\mathcal{P}_2$  and  $\mathcal{P}_3$  involves matching the residues at two different codimension-2 boundaries: the intersections  $L_1 \cap L_2$  and  $L_1 \cap \bar{L}_2$ . Each of these intersections generates a distinct dlog singularities i.e.,  $l_2$  and  $\bar{l}_2$ , preventing the two parent functions from being merged into single one. In contrast, for the bubble case, all parent functions share a single codimension-2 boundary,  $L_1 \cap L_2$ .

Another intriguing feature of the tadpole wavefunction coefficient is that its selective involvement with the system, contrasting with the bubble case. Specifically, only eight basis functions contribute to the canonical differential equations for the tadpole system, despite the hyperplane arrangement suggesting a 10-dimensional vector space. This selective engagement with a subset of the full cohomology space appears to be a recurring pattern as the diagram's complexity increases. For instance, at tree level, the three-site diagram probes only a 16-dimensional subspace within the full 25-dimensional space given by cohomology [8]. This observation highlights that the physical observables possess unique properties absent in generic mathematical constructs.

In the two-site case, we can explicitly identify the components not probed by the tadpole function. The hyperplane arrangement yields twelve canonical forms, corresponding

to all possible triangles bounded by the seven planes in Eq. (3.38), with  $12 = 3 \times 2 \times 2$ . Alongside the eight 2-forms specified in Eq. (3.39), the remaining four 2-forms, defined using the previously established positive orientation, are given by

$$\text{Layer-0: } \quad \bar{\Omega}_{\mathcal{P}_2^u} = \frac{-2(Y_1 - Y_2)}{L_1 L_2 D_2}, \quad \bar{\Omega}_{\mathcal{P}_3^u} = \frac{-2(Y_1 + Y_2)}{L_1 \bar{L}_2 D_3}, \quad (3.45a)$$

$$\text{Layer-1: } \quad \bar{\Omega}_{\mathcal{F}_2^u} = \frac{X_1 - Y_1 + 2Y_2}{T_1 L_2 D_2}, \quad \bar{\Omega}_{\mathcal{F}_3^u} = \frac{X_1 - Y_1 - 2Y_2}{T_1 \bar{L}_2 D_3}, \quad (3.45b)$$

where the corresponding functions are defined as:  $\mathcal{P}_{2,3}^u = \int d\mu \bar{\Omega}_{\mathcal{P}_{2,3}^u}$ ,  $\mathcal{F}_{2,3}^u = \int d\mu \bar{\Omega}_{\mathcal{F}_{2,3}^u}$ . As in the bubble case, the twelve 2-forms (3.7) are actually over complete and subjected to two linear constraints induced by the corresponding triangulation relations (3.9), which reduce the number of the independent basis down to ten. While in the tadpole case, since the two disjoint tree systems have already provided eight independent basis, we will need two relations involving the above four extra 2-forms. Those two linear constraints can be expressed as follows:

$$\begin{aligned} S_1 &= \Delta_{L_1 \bar{L}_2 D_2} - \Delta_{L_1 L_2 D_2} + \Delta_{T_1 L_2 D_2} - \Delta_{T_1 \bar{L}_2 D_2} \\ &= \Delta_{L_1 \bar{L}_2 D_3} - \Delta_{T_1 \bar{L}_2 D_3} + \Delta_{T_1 L_2 D_3} - \Delta_{L_1 L_2 D_3}, \end{aligned} \quad (3.46a)$$

$$\begin{aligned} S_2 &= \Delta_{L_1 L_2 D_2} + \Delta_{T_1 T_2 D_2} - \Delta_{T_1 L_2 D_2} - \Delta_{T_2 L_1 D_2} \\ &= \Delta_{L_1 L_2 D_3} - \Delta_{T_1 L_2 D_3} - \Delta_{T_2 L_1 D_3} + \Delta_{T_1 T_2 D_3}, \end{aligned} \quad (3.46b)$$

where  $S_1$  and  $S_2$  correspond to the blue-shaded and blue rectangular regions in Fig. 4, respectively. Explicitly, the triangulation gives the following nontrivial relations:

$$\bar{\Omega}_{\mathcal{P}_2} - \bar{\Omega}_{\mathcal{P}_2^u} + \bar{\Omega}_{\mathcal{F}_2^u} - \bar{\Omega}_{\mathcal{F}_2} = \bar{\Omega}_{\mathcal{P}_3^u} - \bar{\Omega}_{\mathcal{F}_3^u} + \bar{\Omega}_{\mathcal{F}_3} - \bar{\Omega}_{\mathcal{P}_3}, \quad (3.47a)$$

$$\bar{\Omega}_{\mathcal{P}_2^u} + \bar{\Omega}_{\mathcal{Q}_2} - \bar{\Omega}_{\mathcal{F}_2^u} - \bar{\Omega}_{\tilde{\mathcal{F}}_2} = \bar{\Omega}_{\mathcal{P}_3} - \bar{\Omega}_{\mathcal{F}_3} - \bar{\Omega}_{\tilde{\mathcal{F}}_3} + \bar{\Omega}_{\mathcal{Q}_3}. \quad (3.47b)$$

In principle, we have the flexibility to select any two from these four forms (3.45) to construct a 10-dimensional vector space together with the previously chosen  $\mathbf{F}_2$  and  $\mathbf{F}_3$ . For instance, if we choose  $\bar{\Omega}_{\mathcal{P}_2^u}$  as part of the basis, the total derivative of  $\bar{\Omega}_{\mathcal{P}_2^u}$  can be schematically expressed as:

$$d\mathcal{P}_2^u \sim \mathcal{P}_2^u + \mathcal{F}_2^u + \tilde{\mathcal{F}}_2, \quad (3.48)$$

where  $\mathcal{F}_2^u$  can be further re-expressed in terms of basis functions according to the constraints (3.47). This implies that the differentiation of  $\mathcal{F}_2^u$  couples to the functions  $\{\mathcal{P}_i, \mathcal{F}_j, \mathcal{Q}_k\}$  as dictated by Eq. (3.47b). Consequently, the resulting differential equation for  $\mathcal{P}_2^u$  is not the UT type. Instead, it involves mixing with functions across all hierarchical layers and tree-level systems, leading to increased complexity in the computation. A similar situation arises when choosing  $\mathcal{P}_3^u$  as part of the basis. Thus, to achieve a more efficient formulation, a better choice of basis would include  $\mathcal{F}_2^u$  and  $\mathcal{F}_3^u$ . The differential equations for  $\mathcal{F}_2^u$  and  $\mathcal{F}_3^u$  are derived in Appendix A.2, which we summarize the results as:

$$\begin{aligned} d\mathcal{F}_2^u &= \varepsilon [ \mathcal{F}_2^u d\log(X_1 - Y_1 + 2Y_2) + (\mathcal{F}_2^u - \mathcal{Q}_2) d\log(X_2 + Y_1) \\ &\quad + \mathcal{Q}_2 d\log(X_1 + X_2 + 2Y_2) ], \end{aligned} \quad (3.49a)$$

$$\begin{aligned} d\mathcal{F}_3^u &= \varepsilon [ \mathcal{F}_3^u d\log(X_1 - Y_1 - 2Y_2) + (\mathcal{F}_3^u - \mathcal{Q}_3) d\log(X_2 + Y_1 + 2Y_2) \\ &\quad + \mathcal{Q}_3 d\log(X_1 + X_2) ]. \end{aligned} \quad (3.49b)$$

Together, the basis  $\{\mathcal{P}_2, \mathcal{F}_2, \tilde{\mathcal{F}}_2, \mathcal{F}_2^u, \mathcal{Q}_2, \mathcal{P}_3, \mathcal{F}_3, \tilde{\mathcal{F}}_3, \mathcal{F}_3^u, \mathcal{Q}_3\}$  defines the *whole system* differential equations. The advantage of this choice of basis lies in its simplicity: each DE is of the UT type, and the mixing between functions is significantly minimized. Notably, the two additional basis functions are naturally associated with two disjoint tree systems, ensuring they remain decoupled from one another.

Insights from the study of complete hyperplane arrangements suggest the use of a *tailored basis* for both the tadpole wavefunction and the whole system. The DE structure of  $\{\mathcal{F}_2^u, \mathcal{F}_3^u\}$  being simpler than that of  $\{\mathcal{P}_2^u, \mathcal{P}_3^u\}$  is expected from IBP. By trading the differentiation of external energy for that of the twist variables, the IBP operation of  $\partial_{x_{1,2}}$  generates only  $T_{1,2}$ -poles. Given that  $\mathcal{F}_{2,3}^u$  already contain a single  $T$ -pole, IBP ensures that they primarily couple to themselves and  $Q$ -functions through residue matching. In contrast, since  $\mathcal{P}_{2,3}^u$  do not contain any  $T$ -poles, the  $\mathcal{F}^u$ - and  $\tilde{\mathcal{F}}$ -functions can appear in their DEs. These observations highlight a guiding principle: whenever there is flexibility in choosing a basis, prioritizing canonical forms with more  $T$ -poles can lead to a more efficient and simplified formulation.

Furthermore, our approach of IBP on triangle canonical forms is a special case of the systematic procedure in Ref. [8] using boundary-less linear combination of projective simplex forms. Namely, in integration space  $\mathbb{R}^p$ , we can define projective simplex  $p$ -forms involving all possible  $p$ -tuples of planes as follows:

$$[\mathcal{L}_1 \cdots \mathcal{L}_p] \equiv d\log \mathcal{L}_1 \wedge \cdots \wedge d\log \mathcal{L}_p, \quad (3.50)$$

where the hyperplane  $\mathcal{L}_I \equiv \{T_i, L_j, D_k\}$  and the exterior derivatives are with respect to the internal variables  $x_\alpha$ . In addition, to determine the combinations of Eq. (3.50), we introduce the boundary operator

$$\partial[\mathcal{L}_1 \cdots \mathcal{L}_p] \equiv \sum_{r=1}^p (-1)^{r+1} [\mathcal{L}_1 \cdots \hat{\mathcal{L}}_r \cdots \mathcal{L}_p], \quad (3.51)$$

where the entry below  $\hat{\phantom{x}}$  has been omitted. And the boundary-less means the form is closed under  $\partial$ . Furthermore, these projective  $p$ -forms are the canonical forms of the simplex formed from the intersection of the  $p$  hyperplanes with the plane at infinity  $\mathcal{L}_\infty$ . It is straightforward to verify that the boundary operator satisfies  $\partial^2 = 0$ , and the linear combination of projective  $p$ -forms are closed under  $\partial$  correspond to bounded regions in  $\mathbb{R}^p$ , forming the basis of the twisted integral. Specifically, any  $p$ -simplex (not projective simplex) in  $\mathbb{R}^p$  defined by  $p + 1$  hyperplanes, is exact and hence closed:

$$\Omega_{p\text{-simplex}} = \partial[\mathcal{L}_1 \cdots \mathcal{L}_{p+1}], \quad (3.52)$$

with simplest examples being triangle canonical forms:  $\Omega_\Delta = d\log(\mathcal{L}_i/\mathcal{L}_k) \wedge d\log(\mathcal{L}_j/\mathcal{L}_k)$ . The iterative emerging of  $T$ -poles under IBP corresponds to a formula holds inside of a

twisted integral, which is proved in Ref. [8]:

$$d[\mathcal{L}_1 \cdots \mathcal{L}_p] = \varepsilon \sum_{\alpha} \partial[T_{\alpha} \mathcal{L}_1 \cdots \mathcal{L}_p] \text{dlog} \langle \hat{T}_{\alpha} \hat{\mathcal{L}}_1 \cdots \hat{\mathcal{L}}_p \rangle, \quad (3.53)$$

where we have defined

$$\mathcal{L}_{\alpha} \equiv \hat{\mathcal{L}}_{\alpha} \cdot P, \quad P^I \equiv (1, x_1, \cdots, x_p), \quad \langle \hat{\mathcal{L}}_1 \cdots \hat{\mathcal{L}}_{p+1} \rangle \equiv \det(\hat{\mathcal{L}}_1, \cdots, \hat{\mathcal{L}}_{p+1}). \quad (3.54)$$

The general strategy involves expressing the wavefunction as a closed linear combination of Eq. (3.50), applying Eq. (3.53), and iteratively adding new functions to the basis as new letters appear. However, diverging from this comprehensive approach, we find it more practical in many cases to use bounded simplex regions as the basis. This choice minimizes mixing between different basis elements during differentiation. Explicitly, we employ a bottom-up strategy: we exhaust a priori the independent closed linear combinations of Eq. (3.50) with more twist  $T$ -planes and ensure that each form aligns with the simplex representation in Eq. (3.52).

The tailored basis for tadpole system suggests a *preferred triangle basis* suitable for 2-dimensional two-site systems with general loop number and topology. We denote  $\{\mathbf{P}, \mathbf{F}, \mathbf{Q}\}$  as collections of top, middle, and bottom layer functions respectively, where each represents a distinct type of function within the same category. Below, we state the procedure to exhaust the preferred triangle basis:

- First of all, fully determine  $\mathbf{Q}$ -basis with two  $T$ -planes, expressed as  $\partial[T_1 T_2 D_k]$ , where  $D_k$  iterates over all diagonally-placed lines. Since IBP generates only additional  $T_{1,2}$ -planes, these forms remain self-contained, interacting exclusively within the bottom layer, which ensures they serve as independent bottom-layer functions.
- Next, exhaust mid-layer  $\mathbf{F}$ -basis with one  $T$ -plane and one  $L$ -plane, expressed as  $\partial[T_i L_j D_k]$ . This process involves substituting one  $T$ -plane in  $\mathbf{Q}$ -basis with a parallel  $L$ -plane. Under IBP, any new  $T$ -plane generated will be parallel to  $L_j$ , limiting interactions to forms with the same pole structure. These include the middle-layer functions themselves and the bottom-layer functions already exhausted.
- Finally, identify the top-layer functions in  $\mathbf{P}$ -basis by their exclusive  $L$ -poles after we exhaust all the  $T$ -pole basis, represented as  $\partial[L_i L_j D_k]$ . The number of distinct  $L$ -pairs in remaining basis determines the number of top-layer functions. After applying IBP, these functions generally interact within their layer and with corresponding  $L$ -branches in the middle-layer  $\mathbf{F}$ -functions. Consequently, they serve as parent functions governing the entire differential system.

The distinction in the preferred basis highlights why the tadpole system necessarily develops two parent functions, whereas the bubble system requires only one. For tadpole system, the presence of two types of  $D$ -poles leads to the  $\mathbf{Q}$ -basis being fully defined as  $\{\mathcal{Q}_2, \mathcal{Q}_3\}$ , consisting two elements. The  $\mathbf{F}$ -basis further splits into three distinct  $L$ -branches, each associated with a common  $L$ -pole:

- $\{\tilde{\mathcal{F}}_2, \tilde{\mathcal{F}}_3\}$ , each contains a  $L_1$ -pole;
- $\{\mathcal{F}_2^u, \mathcal{F}_3\}$ , each contains a  $L_2$ -pole;
- $\{\mathcal{F}_2, \mathcal{F}_3^u\}$ , each contains a  $\bar{L}_2$ -pole.

In addition, the existence of two unique  $L$ -pairs,  $(L_1, L_2)$  and  $(L_1, \bar{L}_2)$ , necessitates two parent functions to span the entire system. Specifically,  $\mathcal{P}_3$  interacts with the branches containing  $L_1$ - and  $L_2$ -poles, while  $\mathcal{P}_2$  interacts with the branches containing  $L_1$ - and  $\bar{L}_2$ -poles. In contrast, the bubble system has only one type of  $L$ -pair,  $(L_2, L_2)$ , meaning a single parent function suffices to span the system. Thus, in this case, we can select  $\mathcal{P}_1$ ,  $\mathcal{P}_2$ , or  $\mathcal{P}_3$  as the parent function, as other two functions are linearly dependent by Eq. (3.9).

One of the remarkable features of the preferred triangle basis is its ability to minimize mixing, leading to a maximally block-diagonalized form of  $\tilde{A}$ . For the tadpole system, the basis is ordered as follows:

$$\begin{aligned}\hat{\mathbf{I}}_{\text{tad}} &= (\mathbf{F}_2 \cup \mathbf{F}_3 \cup \{\mathcal{F}_2^u, \mathcal{F}_3^u\})^T \\ &= (\mathcal{P}_2, \mathcal{F}_2, \tilde{\mathcal{F}}_2, \mathcal{F}_2^u, \mathcal{Q}_2, \mathcal{P}_3, \mathcal{F}_3, \tilde{\mathcal{F}}_3, \mathcal{F}_3^u, \mathcal{Q}_3)^T.\end{aligned}\quad (3.55)$$

The integration family (3.55) obeys the following canonical differential equation:

$$d\hat{\mathbf{I}}_{\text{tad}} = \varepsilon \tilde{A}_{\text{tad}} \hat{\mathbf{I}}_{\text{tad}}, \quad (3.56)$$

where the corresponding matrix  $\tilde{A}_{\text{tad}}$  takes the form:

$$\tilde{A}_{\text{tad}} = \begin{pmatrix} l_1 + \bar{l}_2 & l_3 - l_1 & \bar{l}_4 - \bar{l}_2 & 0 & 0 & 0 & 0 & 0 & 0 & 0 & 0 \\ 0 & \bar{l}_2 + l_3 & 0 & 0 & \bar{l}_5 - \bar{l}_2 & 0 & 0 & 0 & 0 & 0 & 0 \\ 0 & 0 & l_1 + \bar{l}_4 & 0 & \bar{l}_5 - l_1 & 0 & 0 & 0 & 0 & 0 & 0 \\ 0 & 0 & 0 & l_2 + l_6 & \bar{l}_5 - l_2 & 0 & 0 & 0 & 0 & 0 & 0 \\ 0 & 0 & 0 & 0 & 2\bar{l}_5 & 0 & 0 & 0 & 0 & 0 & 0 \\ 0 & 0 & 0 & 0 & 0 & l_1 + l_2 & l_3 - l_1 & l_4 - l_2 & 0 & 0 & 0 \\ 0 & 0 & 0 & 0 & 0 & 0 & l_2 + l_3 & 0 & 0 & 0 & l_5 - l_2 \\ 0 & 0 & 0 & 0 & 0 & 0 & 0 & l_1 + l_4 & 0 & 0 & l_5 - l_1 \\ 0 & 0 & 0 & 0 & 0 & 0 & 0 & 0 & l_2 + l_7 & 0 & l_5 - \bar{l}_2 \\ 0 & 0 & 0 & 0 & 0 & 0 & 0 & 0 & 0 & 0 & 2l_5 \end{pmatrix}. \quad (3.57)$$

Further, in Eq. (3.57), the two new letters  $l_6$  and  $l_7$  are given by

$$l_6 = \text{dlog}(X_1 - Y_1 + 2Y_2), \quad l_7 = \text{dlog}(X_1 - Y_1 - 2Y_2). \quad (3.58)$$

The two tree systems are evidently integrable, and the two additional basis, along with their corresponding bottom-level functions  $\{\mathcal{F}_2^u, \mathcal{F}_3^u, \mathcal{Q}_2, \mathcal{Q}_3\}$ , being independently integrable. Therefore, the entire system satisfies the integrability condition. The block-diagonal structure offers a significant advantage: it reduces one of the integrability condition  $\tilde{A} \wedge \tilde{A} = 0$  to a simpler block-wise verification.

To achieve a maximally block-diagonalized form of the matrix  $\tilde{A}$ , it is essential to remain in the triangular basis. This approach ensures that parent functions interact with

the minimum number of  $L$ -branch functions in the middle layer. Such a strategy enables us to efficiently determine whether the entire system is integrable.

As for the tadpole system, using the previously mentioned bottom-up method, we identified two sets of bases,  $\{\mathcal{P}_2, \mathcal{F}_2, \tilde{\mathcal{F}}_2, \mathcal{F}_2^u, \mathcal{Q}_2\}$  and  $\{\mathcal{P}_3, \mathcal{F}_3, \tilde{\mathcal{F}}_3, \mathcal{F}_3^u, \mathcal{Q}_3\}$ . Due to the inability of their associated parent functions to merge, the relevant matrix  $\tilde{A}_{10 \times 10}^{\text{tad}}$  is naturally decomposed into a  $5 \times 5 \oplus 5 \times 5$  block-diagonal form [cf. Eq. (3.57)]. While for the bubble system discussed in Section 3.1, if we traverse from the bottom to the top layer and identify  $\partial[L_1 L_2 D_1]$  i.e.,  $\mathcal{P}_1$  as the single parent function, the matrix  $\tilde{A}_{10 \times 10}^{\text{bub}}$  [cf. Eq. (3.30)] will be block-diagonalized into three submatrices:  $4 \times 4 \oplus 3 \times 3 \oplus 3 \times 3$  with each block corresponding to  $\{\mathcal{P}_1, \mathcal{F}_1, \tilde{\mathcal{F}}_1, \mathcal{Q}_1\}$ ,  $\{\mathcal{F}_2, \tilde{\mathcal{F}}_2, \mathcal{Q}_2\}$  and  $\{\mathcal{F}_3, \tilde{\mathcal{F}}_3, \mathcal{Q}_3\}$ , respectively. However, the selected parent function  $\mathcal{P}_1$  in this case is unphysical. For practical applications, it remains necessary to find an appropriate linear combination to determine the final parent function  $\mathcal{P}$ .

In summary, our comprehensive investigation into loop-level hyperplane arrangements and their associated differential systems uncovers several unique features that are absent at tree level. These findings can be summarized as follows:

- **Ambiguity in Parent Function Definition:** At loop level, defining the parent function based solely on the hyperplane arrangement is ambiguous, and the differential system may involve multiple parent functions. Unlike tree-level systems, where a unique, boundary-less object directly corresponds to the cosmological wavefunction of interest and does not involve twisted planes, this uniqueness does not hold for loop-level cases such as the bubble or tadpole systems. For example, the tadpole system necessarily requires two parent functions to span the system. This ambiguity arises from the parallel  $L$ - and  $D$ -lines in hyperplane arrangements generated by loop diagrams, which contrasts with tree systems where all lines intersect. And this distinction is particularly evident in the tubing approach to wavefunction coefficients; see tree examples in Ref. [8] and loop-level cases in Eq. (4.1) and Eq. (4.21).
- **Reduced Basis Size for Canonical DEs:** At loop level, the number of basis functions relevant to the canonical differential equations is typically smaller than that at tree level with the same number of internal edges. For tree-level systems, the number of basis functions scales as  $4^e$  where  $e$  being the number of the internal edges. In contrast, our analysis shows that the one-loop bubble has 10 basis functions, the tadpole has 8, and the two-site two-loop sunrise has 22, two-site arbitrary loop in bubble type has  $3 \cdot 2^e - 2$  [cf. Eq. (5.6)]. The slower scaling of the relevant vector space dimension at loop level is expected, as the numerous parallel lines appearing in loop hyperplane arrangements make the hyperplane arrangements highly nontrivial, and indicate that the wavefunction of physical interest have special features that distinguish them from generic mathematical objects.



## 4 Kinematic Flow for Two-Site One-Loop Graph

In this section, we apply the tubing graph framework to study the differentiation system for two-site one-loop correlators. For the first time, we extend the tree-level tubing framework [7, 8] to the loop-level. Additionally, we introduce the graphical rules governing loop-level tubings and present a systematic methodology for deriving the associated canonical differential equations which are aligned with the results derived in Section 3. This approach significantly simplifies the derivation process, reducing it to a set of universal and widely applicable principles.

### 4.1 Two-Site One-Loop Bubble

As illustrated in Ref. [1], the wavefunction coefficient for a given graph can be obtained by summing over all possible ways of iteratively dividing the graph into connected tubes<sup>3</sup>, each tube graph associated with the inverse of the sum of its total energies. For two-site one-loop bubble graph, there are two ways to divide the graph into two subgraphs:

$$\tilde{\psi}_{(2,1)}^{\text{bub},(a)} = \text{Diagram} = \frac{1}{X_1+Y_1+Y_2} \times \frac{1}{X_2+Y_1+Y_2} \times \frac{1}{X_1+X_2+2Y_1} \times \frac{1}{X_1+X_2}, \quad (4.1a)$$

$$\tilde{\psi}_{(2,1)}^{\text{bub},(a)} = \text{Diagram} = \frac{1}{X_1+Y_1+Y_2} \times \frac{1}{X_2+Y_1+Y_2} \times \frac{1}{X_1+X_2+2Y_2} \times \frac{1}{X_1+X_2}, \quad (4.1b)$$

where each subgraph contains four tube graphs and the placement of external and internal energies  $\{X_i, Y_j\}$ , please refer to Fig. 1. Here, for the sake of convenience, we have omitted the external legs and late-time boundary. Further, by summing over the two contributions in Eq. (4.1), we can obtain the full wavefunction coefficient in flat spacetime,  $\tilde{\psi}_{(2,1)}^{\text{bub}}$ , which aligns with Eq. (3.1).

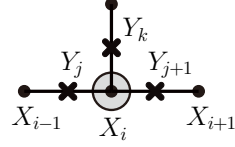
Given that tubes can reflect the singularities, we aim to establish a connection between tubings and the canonical differential equations. To achieve it, we use the property that kinematic data can flow along the internal lines, driving the evolution of the tubes. And we will adopt a similar approach as established in the graphs at tree level [8], where the cross signs “ $\times$ ” are dressed on the internal lines, which these marks indicate that the kinematic variables flow along these intermediate edges. Then, the letters appearing in the canonical differential equations are then depicted as the connected tubes, which are formed by encircling the vertices or both of the vertices and cross signs in a graph. These are characterized as follows:

- If a tube graph encircles only a single vertex, it corresponds to a dlog form of the sum of the energy associated with that vertex and the all of the energies associated with the internal lines intersected by the tube. For example, consider a graph with a

---

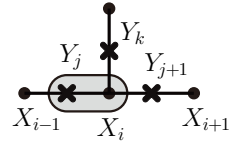
<sup>3</sup>Different conventions exist regarding whether the outermost tube, which contains all vertices, should be included. Such as Refs. [14–16] choose to omit it, whereas in our work, we consistently include it.

3-vertex, where the tube only enclose the vertex  $X_i$  and intersects the three internal legs. Thus, letter corresponding to the tube is given by

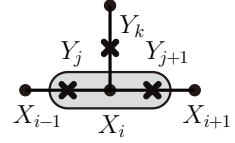


$$= \text{dlog}(X_i + Y_j + Y_{j+1} + Y_k). \quad (4.2)$$

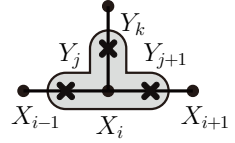
- If the tube graph encircles both a vertex and its adjacent internal lines marked with cross signs, the corresponding dlog form requires flipping the sign of the energies associated with those marked internal lines. The following three examples illustrate different tubes and their corresponding letters:



$$= \text{dlog}(X_i - Y_j + Y_{j+1} + Y_k), \quad (4.3a)$$

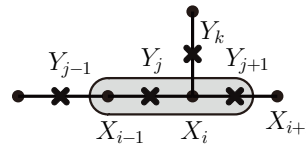


$$= \text{dlog}(X_i - Y_j - Y_{j+1} + Y_k), \quad (4.3b)$$



$$= \text{dlog}(X_i - Y_j - Y_{j+1} - Y_k). \quad (4.3c)$$

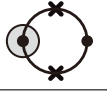










- If the tube graph contains more than one vertex, then the energies associated with the marked internal lines between any two enclosed vertices will vanish in its associated dlog expression. For instance, in the diagram below, the letter corresponding to the tube is given by



$$= \text{dlog}(X_{i-1} + X_i + Y_{j-1} - Y_{j+1} + Y_k). \quad (4.4)$$








Therefore, all the letters appearing in the canonical differential equations of tow-site one-loop bubble-type wavefunction coefficient [cf. (3.29)] can be represented as marked tubing graphs which are summarized in Table 1.

The functions belonging to the integral family (3.11) can be systematically represented using a framework of complete tubes [7, 8]. In this framework, tube graphs associated with the parent function are characterized by the absence of cross signs, reflecting their simplest and most fundamental structure. Conversely, tube graphs representing descendant functions incorporate one or more cross signs, indicating the addition of specific contributions or constraints that differentiate them from their parent. These functions are

$l_1$		$\text{dlog}(X_1+Y_1+Y_2)$	$l_2$		$\text{dlog}(X_2+Y_1+Y_2)$
$l_3$		$\text{dlog}(X_1+Y_1-Y_2)$	$l_4$		$\text{dlog}(X_2+Y_1-Y_2)$
$l_5$		$\text{dlog}(X_1-Y_1+Y_2)$	$l_6$		$\text{dlog}(X_2-Y_1+Y_2)$
$l_7$		$\text{dlog}(X_1-Y_1-Y_2)$	$l_8$		$\text{dlog}(X_2-Y_1-Y_2)$
$l_9$		$\text{dlog}(X_1+X_2+2Y_1)$	$l_{10}$		$\text{dlog}(X_1+X_2+2Y_2)$
$l_{11}$		$\text{dlog}(X_1+X_2)$			

**Table 1.** The alphabet for the two-site one-loop bubble-type wavefunction coefficient where the letters  $l_i = \text{dlog}(w_i)$ .

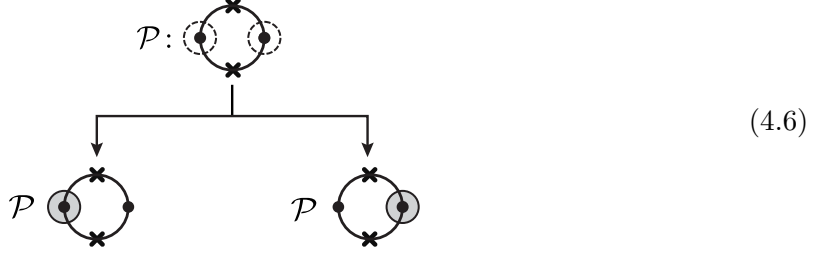
naturally organized into three distinct hierarchical layers, as detailed in Eq. (3.6). Their explicit forms can be expressed as follows:

Layer-0		$\mathcal{P}$					
Layer-1		$\tilde{\mathcal{F}}_1$		$\tilde{\mathcal{F}}_2$		$\tilde{\mathcal{F}}_3$	(4.5)
Layer-2		$\mathcal{Q}_1$		$\mathcal{Q}_2$		$\mathcal{Q}_3$	

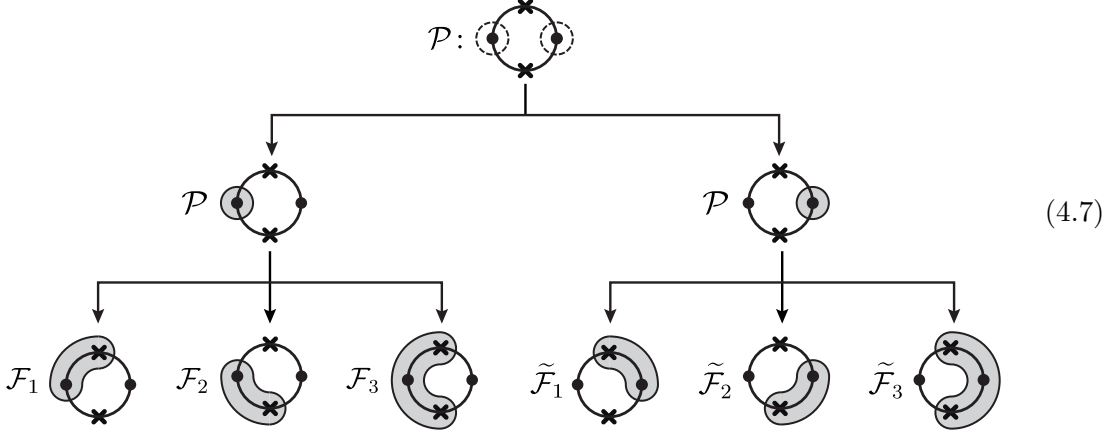
where they are categorized into three layers according to Eq. (3.6). In addition, in Eq. (4.5), dashed lines are used to depict tube graphs, serving as “seeds” that form the foundational building blocks for constructing more intricate structures. Activating these seed tubes sequentially will generate new branches, collectively forming a “family tree”. Each activated tube is corresponding to a specific letter, enabling a systematic derivation of the canonical DEs governing the system.

Now, we focus on the graph of the parent function  $\mathcal{P}$  to show how it works. We will construct the family tree for  $\mathcal{P}$  step by step. Firstly, activating the tubes of  $\mathcal{P}$  generates

two branches, each one is corresponding to a distinct letter,



where for each branch in the tree, we have also assigned the function associated with the tube graph. Next, each activated tube in Eq. (4.6) that does not contain a cross sign can “grow” to enclose all of its adjacent cross signs in all possible ways. Each distinct growth pathway generates a new branch. Collecting all branches, we can obtain the family tree for the parent function  $\mathcal{P}$  as follows:



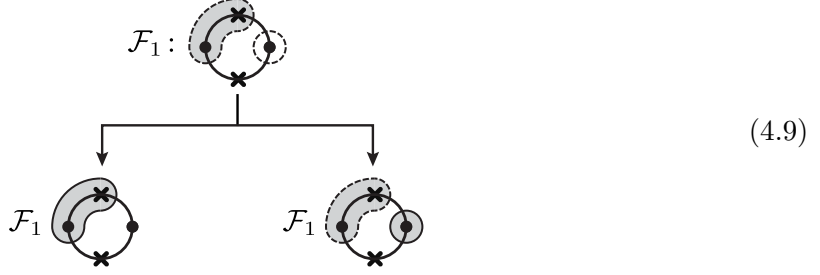
where we have assigned the descendant functions  $\{\mathcal{F}_i\}$  and  $\{\tilde{\mathcal{F}}_i\}$  associated with the tubes in the third layer of Eq. (4.7). Finally, to obtain the differential equation for  $\mathcal{P}$  from the family tree (4.7), we multiply each tube (letter) by the difference between its corresponding function and the sum of the functions associated with all its descendant tube graphs, scaled by a constant factor  $\varepsilon$ :

$$\begin{aligned}
 d\mathcal{P} &= \varepsilon \left[ \left( \mathcal{P} - \sum_{i=1}^3 \mathcal{F}_i \right) l_1 + \left( \mathcal{P} - \sum_{i=1}^3 \tilde{\mathcal{F}}_i \right) l_2 + \sum_{i=1}^3 \mathcal{F}_i l_{2i+1} + \sum_{i=1}^3 \tilde{\mathcal{F}}_i l_{2i+2} \right] \\
 &= \varepsilon \left[ \mathcal{P}(l_1 + l_2) + \mathcal{F}_1(l_3 - l_1) + \tilde{\mathcal{F}}_1(l_4 - l_2) + \mathcal{F}_2(l_5 - l_1) + \tilde{\mathcal{F}}_2(l_6 - l_2) \right. \\
 &\quad \left. + \mathcal{F}_3(l_7 - l_1) + \tilde{\mathcal{F}}_3(l_8 - l_2) \right], \tag{4.8}
 \end{aligned}$$

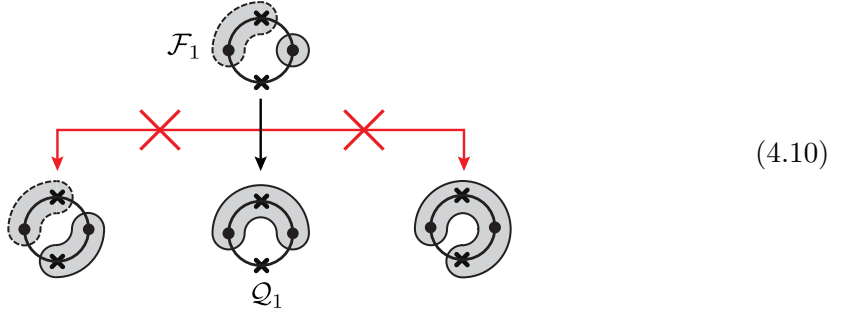
where the letters  $\{l_i\}$  are summarized in Table 1. As we proceed with the activation and growth process, we can see each newly activated tube generates additional branches, expanding the family tree and manifesting the structure underlying the differential equations through the graphical representation.

Next, we move to study the descendant functions  $\mathcal{F}_1$  and  $\tilde{\mathcal{F}}_1$  in layer-1 of Eq. (4.7). For the function  $\mathcal{F}_1$ , the two dashed tubes in the graph of  $\mathcal{F}_1$  can be activated independently,

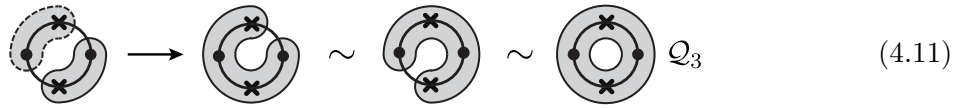
forming two different branches:



where in the second branch of Eq. (4.9), the activated tube can continue to grow and enclose its adjacent cross signs in three different ways:



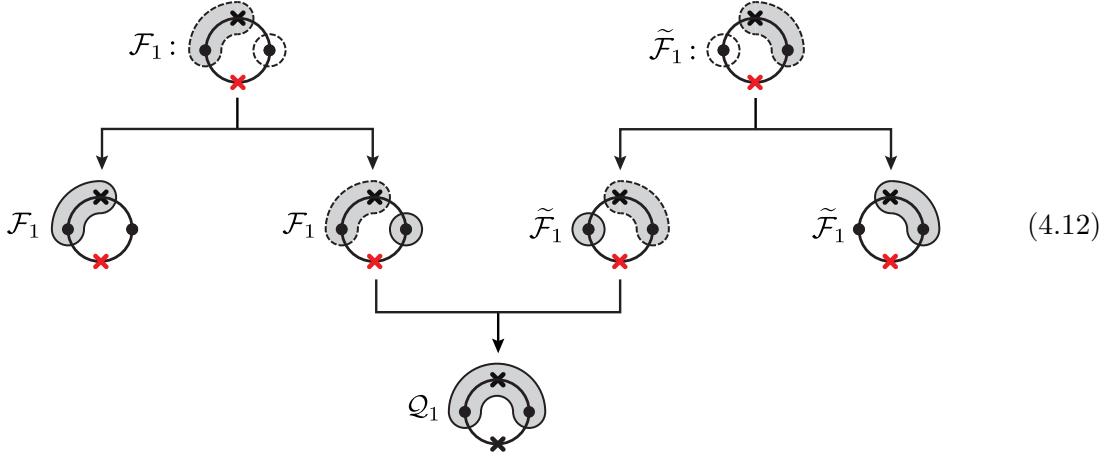
However, notice that in Eq. (4.10), we have used red arrows to mark the first and third branches, highlighting that the activated tube cannot evolve further into these two branches. These restrictions arise because, in the first branch of Eq. (4.10), the newly formed tube will “merge” with its neighboring tube to form a larger tube. Meanwhile, in the third branch of Eq. (4.10), the activated tube directly encloses the cross signs above and below it. As a result, the tube graphs evolve in the first and third branch are topologically equivalent:



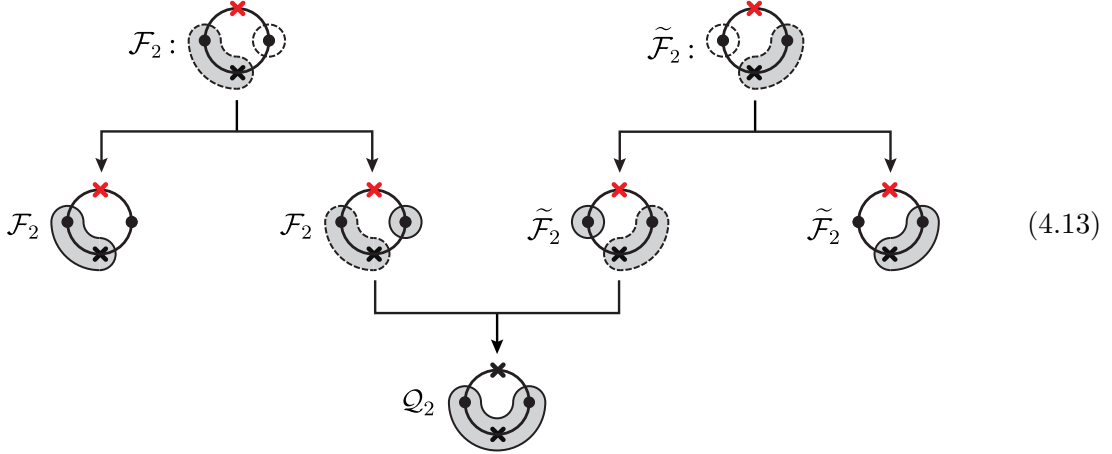
where the final descendant tube of Eq. (4.11) is associated with the function  $\mathcal{Q}_3$  which should correspond to the ultimate tube graph in the family trees of  $\mathcal{F}_3$  and  $\tilde{\mathcal{F}}_3$  (we will discuss it later). Further, the subsystem of hyperplane arrangement for  $\mathcal{F}_1$  is solely related to the planes  $\{T_1, L_2, D_1\}$  [cf. Eq. (3.7b)]. However, the final tube in Eq. (4.11) is related to the planes  $\{T_1, T_2, D_3\}$  [cf. Eq. (3.7d)], and  $D_3$  clearly should not appear in the hyperplane system associated with  $\mathcal{F}_1$ . Therefore,  $\mathcal{F}_1$  can only evolve along the second branch in Eq. (4.11).

For the function  $\tilde{\mathcal{F}}_1$ , we can construct its associated family tree using a method similar to that of  $\mathcal{F}_1$ , so we will ignore the detailed process here. Consequently, the complete family

trees for  $\mathcal{F}_1$  and  $\tilde{\mathcal{F}}_1$  are constructed as follows:



where the crosses signs marked in red color indicate that these crosses are prevented to be enclosed by the activated tube. Similarly, due to the presence of symmetry, the construction of the family trees for  $\mathcal{F}_2$  and  $\tilde{\mathcal{F}}_2$  closely mirrors that of  $\mathcal{F}_1$  and  $\tilde{\mathcal{F}}_1$ . Therefore, we omit the step-by-step derivation and summarize the results as follows:



Hence, the canonical DEs associated with the descendant functions  $\{\mathcal{F}_1, \tilde{\mathcal{F}}_1, \mathcal{F}_2, \tilde{\mathcal{F}}_2\}$  can be easily read from the family trees (4.12)-(4.13):

$$d\mathcal{F}_1 = \varepsilon[(\mathcal{F}_1 - \mathcal{Q}_1)l_2 + \mathcal{F}_1 l_3 + \mathcal{Q}_1 l_9] = \varepsilon[\mathcal{F}_1(l_2 + l_3) + \mathcal{Q}_1(l_9 - l_2)], \quad (4.14a)$$

$$d\tilde{\mathcal{F}}_1 = \varepsilon[(\tilde{\mathcal{F}}_1 - \mathcal{Q}_1)l_1 + \mathcal{F}_1 l_4 + \mathcal{Q}_1 l_9] = \varepsilon[\tilde{\mathcal{F}}_1(l_1 + l_4) + \mathcal{Q}_1(l_9 - l_1)], \quad (4.14b)$$

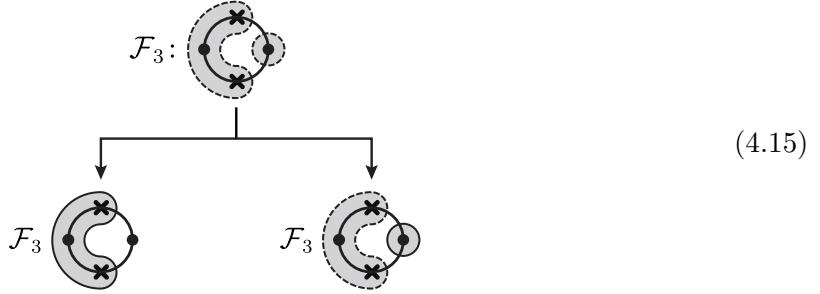
$$d\mathcal{F}_2 = \varepsilon[(\mathcal{F}_2 - \mathcal{Q}_2)l_2 + \mathcal{F}_2 l_5 + \mathcal{Q}_2 l_{10}] = \varepsilon[\mathcal{F}_2(l_2 + l_5) + \mathcal{Q}_2(l_{10} - l_2)], \quad (4.14c)$$

$$d\tilde{\mathcal{F}}_2 = \varepsilon[(\tilde{\mathcal{F}}_2 - \mathcal{Q}_2)l_1 + \tilde{\mathcal{F}}_2 l_6 + \mathcal{Q}_2 l_{10}] = \varepsilon[\tilde{\mathcal{F}}_2(l_1 + l_6) + \mathcal{Q}_2(l_{10} - l_1)], \quad (4.14d)$$

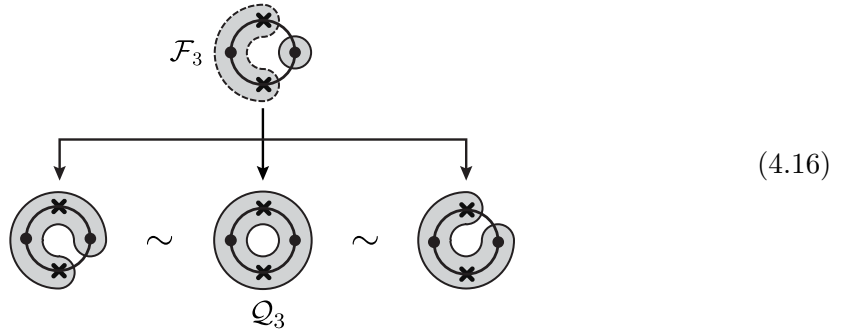
where the letters  $\{l_i\}$  are given in Table 1. Here, the rules for generating the family trees of  $\{\mathcal{F}_1, \tilde{\mathcal{F}}_1, \mathcal{F}_2, \tilde{\mathcal{F}}_2\}$  differ slightly from those at the tree level. This is because, within our chosen basis, the family tree for each subsystem is independent and does not mix with others. Hence, some graphs that are unique in one family tree do not appear in other

family trees. This feature can also be clearly derived through the analysis of hyperplane arrangements in Section 3.1.

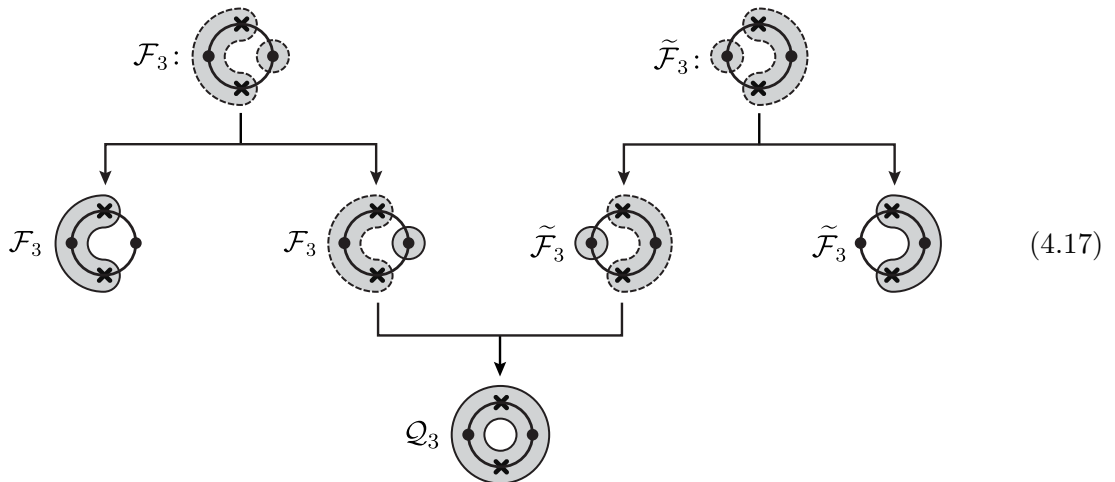
Subsequently, we concentrate on studying the last two descendant functions  $\mathcal{F}_3$  and  $\tilde{\mathcal{F}}_3$  in layer-1. Again, for  $\mathcal{F}_3$ , the two dashed tubes in the graph of  $\mathcal{F}_3$  can be activated independently, forming two distinct branches:



In the second branch of Eq. (4.15), the activated tube can continue to grow and encloses the cross sign above, below, or both, thereby forming three branches:



where those three branches are topologically equivalent, reducing the final descendant tube graph to a single configuration, the second branch in Eq. (4.16). A similar approach applies to  $\tilde{\mathcal{F}}_3$ , yielding a parallel family tree. In summary, the complete family trees associated with  $\mathcal{F}_3$  and  $\tilde{\mathcal{F}}_3$  are represented as follows:



Thus, the canonical DEs associated with the functions  $\mathcal{F}_3$  and  $\tilde{\mathcal{F}}_3$  can be obtained from the family tree (4.17) as follows:

$$d\mathcal{F}_3 = \varepsilon[(\mathcal{F}_3 - \mathcal{Q}_3)l_2 + \mathcal{F}_3l_7 + \mathcal{Q}_3l_{11}] = \varepsilon[\mathcal{F}_3(l_2 + l_7) + \mathcal{Q}_3(l_{11} - l_2)], \quad (4.18a)$$

$$d\tilde{\mathcal{F}}_3 = \varepsilon[(\tilde{\mathcal{F}}_3 - \mathcal{Q}_3)l_1 + \tilde{\mathcal{F}}_3l_8 + \mathcal{Q}_3l_{11}] = \varepsilon[\tilde{\mathcal{F}}_3(l_1 + l_8) + \mathcal{Q}_3(l_{11} - l_1)], \quad (4.18b)$$

where the letters  $\{l_i\}$  can be found in Table 1.

Finally, we analyze the three descendant functions  $\mathcal{Q}_1$ ,  $\mathcal{Q}_2$  and  $\mathcal{Q}_3$  in layer-2 of Eq. (4.7). In this scenario, the graphs associated with  $\{\mathcal{Q}_i\}$  are enclosed by a single tube that becomes activated:

(4.19)

where the factor 2 in the second layer of Eq. (4.19) emerges from the enclosure of two vertices within the activated tube. Hence, by referencing the family trees in Eq. (4.19), we can derive the canonical DEs for  $\{\mathcal{Q}_i\}$  as follows:

$$d\mathcal{Q}_1 = 2\varepsilon\mathcal{Q}_1l_9, \quad d\mathcal{Q}_2 = 2\varepsilon\mathcal{Q}_2l_{10}, \quad d\mathcal{Q}_3 = 2\varepsilon\mathcal{Q}_3l_{11}. \quad (4.20)$$

Collecting Eqs. (4.14), (4.18) and (4.19), we can check that they are consistent with the results (3.28) derived by using the methods of hyperplane arrangement and IBP.

## 4.2 Two-Site One-Loop Tadpole

Similar to the bubble case, for the two-site one-loop tadpole graph, there are also two ways to divide the graph into two subgraphs composed by connected tubes:

$$\tilde{\psi}_{(2,1)}^{\text{tad},(a)} = \text{Diagram (a)} = \frac{1}{X_1+Y_1} \times \frac{1}{X_2+Y_1+2Y_2} \times \frac{1}{X_1+X_2+2Y_2} \times \frac{1}{X_1+X_2}, \quad (4.21a)$$

$$\tilde{\psi}_{(2,1)}^{\text{tad},(b)} = \text{Diagram (b)} = \frac{1}{X_1+Y_1} \times \frac{1}{X_2+Y_1+2Y_2} \times \frac{1}{X_2+Y_1} \times \frac{1}{X_1+X_2}, \quad (4.21b)$$

where each subgraph contains four tubes. Summing over the two contributions in Eq. (4.21), we can obtain the full wavefunction coefficient in flat spacetime,  $\tilde{\psi}_{(2,1)}^{\text{tad}}$ , which is consistent with Eq. (3.36).

Subsequently, to examine the differential system for the tadpole case, we consider the graphs dressed with cross signs on their internal edges. These markings systematically generate all the relevant letters associated with tubes, as summarized in Table 2.



$l_1$		$\text{dlog}(X_1 + Y_1)$	$l_2$		$\text{dlog}(X_2 + Y_1)$
$l_3$		$\text{dlog}(X_1 - Y_1)$	$l_4$		$\text{dlog}(X_2 - Y_1)$
$l_5$		$\text{dlog}(X_1 + X_2)$			
$\bar{l}_2$		$\text{dlog}(X_2 + Y_1 + 2Y_2)$	$\bar{l}_4$		$\text{dlog}(X_2 - Y_1 + 2Y_2)$
$\bar{l}_5$		$\text{dlog}(X_1 + X_2 + 2Y_2)$			

**Table 2.** The alphabet for two-site one-loop tadpole-type wavefunction coefficient consists of letters  $l_i = \text{dlog}(w_i)$  and  $\bar{l}_j = \text{dlog}(\bar{w}_j)$ , excluding  $\{l_6, l_7\}$ , as they do not contribute the physical system.

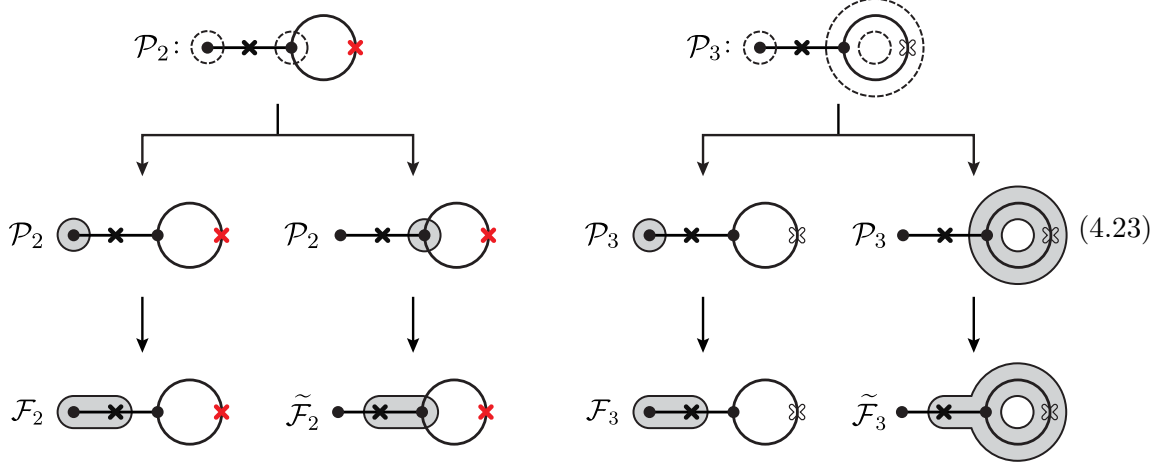
The kinematic flow method, when applied to the tadpole case, is specifically suited for investigating the physical integral family discussed in Section 3.2. However, it does not provide a framework for addressing the unphysical components of the integral family. The eight physical functions within the integral family  $\mathbf{I}_{\text{tad}} = (\mathbf{F}_2 \cup \mathbf{F}_3)^T$  can be categorized into three distinct layers, each characterized by its own set of associated tubing graphs, which serve as graphical representations. These tubing graphs are explicitly illustrated as follows:

Layer-0					
Layer-1					(4.22)
Layer-2					

where there are two distinct parent function  $\mathcal{P}_2$  and  $\mathcal{P}_3$  in layer-0 as discussed in Section 3.2. Further, for the functions  $\{\mathcal{P}_2, \mathcal{F}_2, \tilde{\mathcal{F}}_2\}$ , the red-marked cross signs indicate that these cross signs cannot be enclosed by the activated tube during the generation of the family tree. And for the functions  $\{\mathcal{P}_3, \mathcal{F}_3, \tilde{\mathcal{F}}_3\}$ , the hollow cross signs represent “ineffective” markers, meaning that tubes containing these hollow cross signs adhere to the same growth rules as those without any cross signs, which they will enclose their adjacent solid cross signs. This ensures  $\mathbf{F}_2$  and  $\mathbf{F}_3$  can evolve independently without any mixing.

Now, let us analyze the kinematic flow structure of the function corresponding to the

tadpole graph. First, for the layer-1 functions, there are two distinct parent functions  $\mathcal{P}_2$  and  $\mathcal{P}_3$ , each of them contains two seed tubes. These seed tubes can be activated and then enclose their adjacent cross signs, forming two distinct branches:



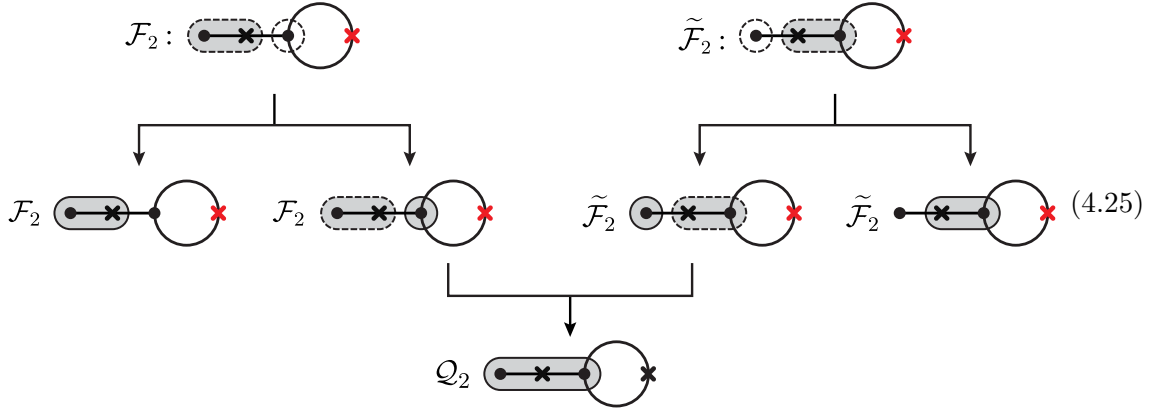
In the second branch of  $\mathcal{P}_2$ , the activated tube can only enclose the black-marked cross sign; otherwise, the resulting graph would mix into the family tree of  $\mathcal{P}_3$ . On the other hand, in the second branch of  $\mathcal{P}_3$ , the presence of a hollow cross sign allows the activated tube to enclose one additional adjacent cross sign. Therefore, the canonical DEs are obtained according to the family trees (4.23)

$$\begin{aligned} d\mathcal{P}_2 &= \varepsilon [(\mathcal{P}_2 - \mathcal{F}_2)l_1 + (\mathcal{P}_2 - \tilde{\mathcal{F}}_2)\bar{l}_2 + \mathcal{F}_2l_3 + \tilde{\mathcal{F}}_2\bar{l}_4] \\ &= \varepsilon [\mathcal{P}_2(l_1 + \bar{l}_2) + \mathcal{F}_2(l_3 - l_1) + \tilde{\mathcal{F}}_2(\bar{l}_4 - \bar{l}_2)], \end{aligned} \quad (4.24a)$$

$$\begin{aligned} d\mathcal{P}_3 &= \varepsilon [(\mathcal{P}_3 - \mathcal{F}_3)l_1 + (\mathcal{P}_3 - \tilde{\mathcal{F}}_3)l_2 + \mathcal{F}_3l_3 + \tilde{\mathcal{F}}_3l_4] \\ &= \varepsilon [\mathcal{P}_3(l_1 + l_2) + \mathcal{F}_3(l_3 - l_1) + \tilde{\mathcal{F}}_3(l_4 - l_2)], \end{aligned} \quad (4.24b)$$

where the letters  $\{l_i, \bar{l}_j\}$  are given in Table. 2. From this, we can observe that the types of letters associated with  $\mathcal{P}_2$  and  $\mathcal{P}_3$  are not entirely the same, as they contain  $\bar{l}_2$  and  $l_2$  respectively. This distinction prevents  $\mathcal{P}_2$  and  $\mathcal{P}_3$  from being merged into a single function unlike the bubble case, where all parent functions share the same set of letters.

Next, for the descendant functions  $\mathcal{F}_2$  and  $\tilde{\mathcal{F}}_2$  in layer-1, their corresponding family trees are given by

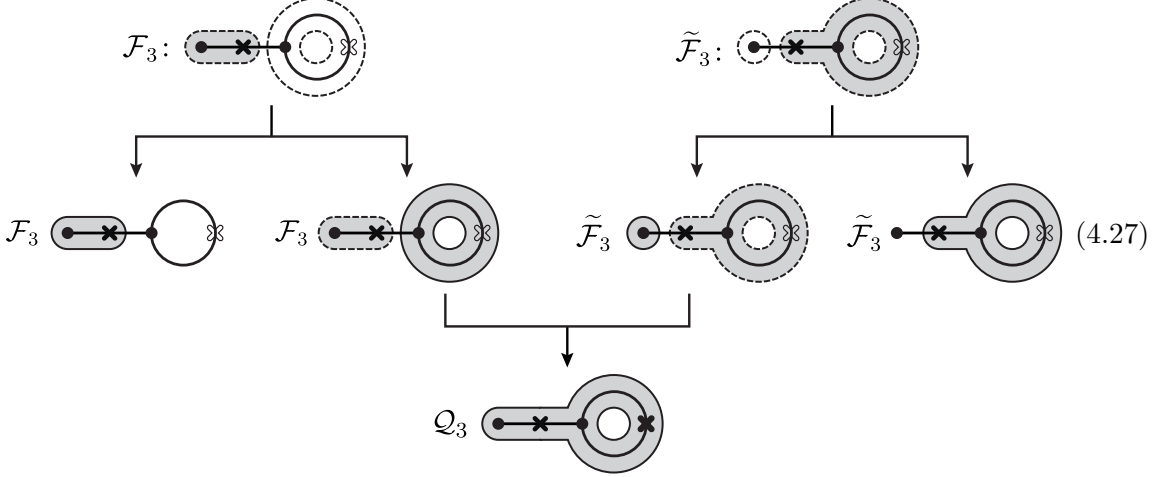


where the corresponding canonical DEs can be obtained from the family trees (4.25) as follows:

$$d\mathcal{F}_2 = \varepsilon [(\mathcal{F}_2 - \mathcal{Q}_2)\bar{l}_2 + \mathcal{F}_2 l_3 + \mathcal{Q}_2 \bar{l}_5] = \varepsilon [\mathcal{F}_2(\bar{l}_2 + l_3) + \mathcal{Q}_2(\bar{l}_5 - \bar{l}_2)], \quad (4.26a)$$

$$d\tilde{\mathcal{F}}_2 = \varepsilon [(\tilde{\mathcal{F}}_2 - \mathcal{Q}_2)l_1 + \tilde{\mathcal{F}}_2 \bar{l}_4 + \mathcal{Q}_2 \bar{l}_5] = \varepsilon [\tilde{\mathcal{F}}_2(l_1 + \bar{l}_4) + \mathcal{Q}_2(\bar{l}_5 - l_1)]. \quad (4.26b)$$

Similarly, for the descendant functions  $\mathcal{F}_3$  and  $\tilde{\mathcal{F}}_3$  in layer-1, their corresponding family tree are given by

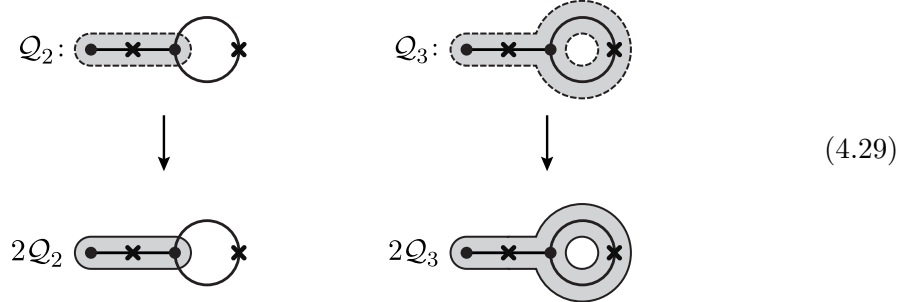


where the canonical DEs can be read from the Eq. (4.27) as follows:

$$d\mathcal{F}_3 = \varepsilon [(\mathcal{F}_3 - \mathcal{Q}_3)l_2 + \mathcal{F}_3 l_3 + \mathcal{Q}_3 l_5] = \varepsilon [\mathcal{F}_3(l_2 + l_3) + \mathcal{Q}_3(l_5 - l_2)], \quad (4.28a)$$

$$d\tilde{\mathcal{F}}_3 = \varepsilon [(\tilde{\mathcal{F}}_3 - \mathcal{Q}_3)l_1 + \tilde{\mathcal{F}}_3 l_4 + \mathcal{Q}_3 l_5] = \varepsilon [\tilde{\mathcal{F}}_3(l_1 + l_4) + \mathcal{Q}_3(l_5 - l_1)]. \quad (4.28b)$$

Finally, for the two descendant functions  $\mathcal{Q}_2$  and  $\mathcal{Q}_3$  in layer-2, each graph associated with them only contains a single tube which can be activated as:



where the canonical DEs can be obtained from the family tree (4.29) as follows:

$$d\mathcal{Q}_2 = 2\varepsilon \mathcal{Q}_2 \bar{l}_5, \quad d\mathcal{Q}_3 = 2\varepsilon \mathcal{Q}_3 l_5. \quad (4.30)$$

Finally, all the canonical differential equations obtained from the family trees are found to be in complete agreement with the results derived in Section 3.2.1. This consistency not only confirms the validity of our approach but also emphasizes the efficiency of the kinematic flow method in systematically capturing the underlying structures of the equations at loop level. Further, it strengthens the broader applicability of this framework to more complex scenarios in future research.

## 5 Analysis for Two-Site Higher Loop Graph

In Sections 3-4, we conducted a detailed study of the one-loop case. In this section, we briefly analyze a few cases with  $L > 1$  to demonstrate that our method for the two-site one-loop bubble diagram can be effectively generalized to higher-loop orders.

We first study case of the two-site two-loop sunset-type wavefunction coefficient. The FRW wavefunction coefficient is computed as follows:

$$\begin{aligned} \psi_{(2,2)}^{\text{sun}} &= 8Y_1Y_2Y_3 \int \frac{d\mu}{L_1L_2D_7} \left[ \frac{1}{D_1} \left( \frac{1}{D_4} + \frac{1}{D_5} \right) + \frac{1}{D_2} \left( \frac{1}{D_4} + \frac{1}{D_6} \right) + \frac{1}{D_3} \left( \frac{1}{D_5} + \frac{1}{D_6} \right) \right], \\ &\equiv \int d\mu \bar{\Omega}_{\mathcal{P}}, \end{aligned} \quad (5.1)$$

where  $d\mu$  is introduced in Eq. (3.6) and the divisors (associated with relative singularities) are defined as follows:

$$\begin{aligned} L_1 &= x_1 + X_1 + Y_1 + Y_2 + Y_3, & L_2 &= x_2 + X_2 + Y_1 + Y_2 + Y_3, \\ D_1 &= x_1 + x_2 + X_1 + X_2 + 2Y_1, & D_2 &= x_1 + x_2 + X_1 + X_2 + 2Y_2, \\ D_3 &= x_1 + x_2 + X_1 + X_2 + 2Y_3, & D_4 &= x_1 + x_2 + X_1 + X_2 + 2(Y_1 + Y_2), \\ D_5 &= x_1 + x_2 + X_1 + X_2 + 2(Y_1 + Y_3), & D_6 &= X_1 + X_2 + x_1 + x_2 + 2(Y_2 + Y_3), \\ D_7 &= x_1 + x_2 + X_1 + X_2. \end{aligned} \quad (5.2)$$

And the Feynman diagram and the associated hyperplane arrangement for two-site two-loop sunset-type wavefunction coefficient are illustrated in Fig. 5.

Inspecting the hyperplane arrangement, there are twenty two independent chambers, each one corresponds to an independent function. All the functions are organized into three distinct layers, as presented in Eq. (B.1), and they constitute the integration family as:

$$\mathbf{I}_{\text{sun}} = (\mathcal{P}, \mathcal{F}_1, \dots, \mathcal{F}_7, \tilde{\mathcal{F}}_1, \dots, \tilde{\mathcal{F}}_7, \mathcal{Q}_1, \dots, \mathcal{Q}_7)^T. \quad (5.3)$$

Here, in Eq. (5.3), the layer-0 comprises a single parent function  $\mathcal{P}$ , marked in red, layer-1 consists of fourteen descendant functions  $\{\mathcal{F}_i, \tilde{\mathcal{F}}_i\}$ , marked in blue, while the layer-2

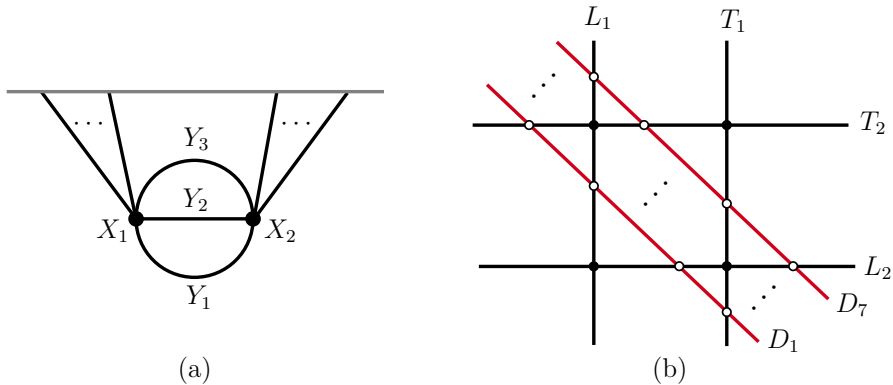


**Figure 5.** (a). The Feynman diagram for the two-site two-loop sunset-type wavefunction coefficient. (b). The hyperplane arrangement for the two-site two-loop sunset-type wavefunction coefficient.



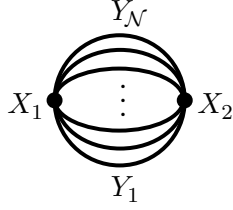


**Figure 6.** The Feynman diagram for the two-site  $L$ -loop bubble-type graph with  $\mathcal{N}$  internal lines where the late-time boundary and external legs are omitted.

At the two-site two-loop level, three additional topologies emerge, each involving one or more tadpoles. As highlighted in the main text, these cases exemplify scenarios where the DEs unavoidably involve multiple parent functions and fail to fully span the hyperplane system. In the rest of this section, we demonstrate that the preferred triangle basis offers a systematic and transparent approach to address these more intricate cases. It enables us to reveal tree-level factorization, quantify the number of functions in each layer, and systematically organize the structure of the  $\tilde{A}$  matrix.

**Dumbbell** One of the two-loop systems demonstrating tree-level factorization analogous to the one-loop tadpole case is the two-tadpole dumbbell diagram, depicted in Fig. 7(a). The wavefunction coefficient is computed as follows:

$$\begin{aligned} \psi_{(2,2)}^{\text{dbl}} &= 8Y Y_1 Y_2 \int \frac{d\mu}{\bar{L}_1 \bar{L}_2 D_3} \left( \frac{1}{L_1 L_2} + \frac{1}{L_1 D_2} + \frac{1}{L_2 D_1} + \frac{1}{D_1 D_4} + \frac{1}{D_2 D_4} \right) \\ &\equiv \int d\mu \bar{\Omega}_{\mathcal{P}_{\text{dbl}}}, \end{aligned} \quad (5.8)$$

where the hyperplanes are defined as follows:

$$\begin{aligned} L_1 &= x_1 + X_1 + Y, & L_2 &= x_2 + X_2 + Y, \\ \bar{L}_1 &= x_1 + X_1 + Y + 2Y_1, & \bar{L}_2 &= x_2 + X_2 + Y + 2Y_2, \\ D_1 &= x_1 + x_2 + X_1 + X_2 + 2Y_1, & D_2 &= x_1 + x_2 + X_1 + X_2 + 2Y_2, \\ D_3 &= x_1 + x_2 + X_1 + X_2, & D_4 &= x_1 + x_2 + X_1 + X_2 + 2(Y_1 + Y_2). \end{aligned} \quad (5.9)$$

Evaluating every codimension-2 residue of the integrand within hyperplane arrangement [white points shown in Fig. 7(b)], we identify the shaded region whose canonical form is  $\bar{\Omega}_{\mathcal{P}_{\text{dbl}}}$ . The shaded regions provide a visual representation of the physical wavefunction coefficient on the hyperplane configuration. Its triangulation further indicates that the wavefunction coefficient can be decomposed into a linear combination of four tree-level subsystems as:

$$\bar{\Omega}_{\mathcal{P}_{\text{dbl}}} = \bar{\Omega}_{\mathcal{P}_1} + \bar{\Omega}_{\mathcal{P}_2} - \bar{\Omega}_{\mathcal{P}_3} - \bar{\Omega}_{\mathcal{P}_4}. \quad (5.10)$$

In Eq. (5.10),  $\bar{\Omega}_{\mathcal{P}_i}$  can be expressed in terms of Eq. (5.9) as follows:

$$\bar{\Omega}_{\mathcal{P}_1} = \frac{-2Y}{\bar{L}_1 L_2 D_1}, \quad \bar{\Omega}_{\mathcal{P}_2} = \frac{-2Y}{L_1 \bar{L}_2 D_2}, \quad \bar{\Omega}_{\mathcal{P}_3} = \frac{-2Y}{L_1 L_2 D_3}, \quad \bar{\Omega}_{\mathcal{P}_4} = \frac{-2Y}{\bar{L}_1 \bar{L}_2 D_4}, \quad (5.11)$$

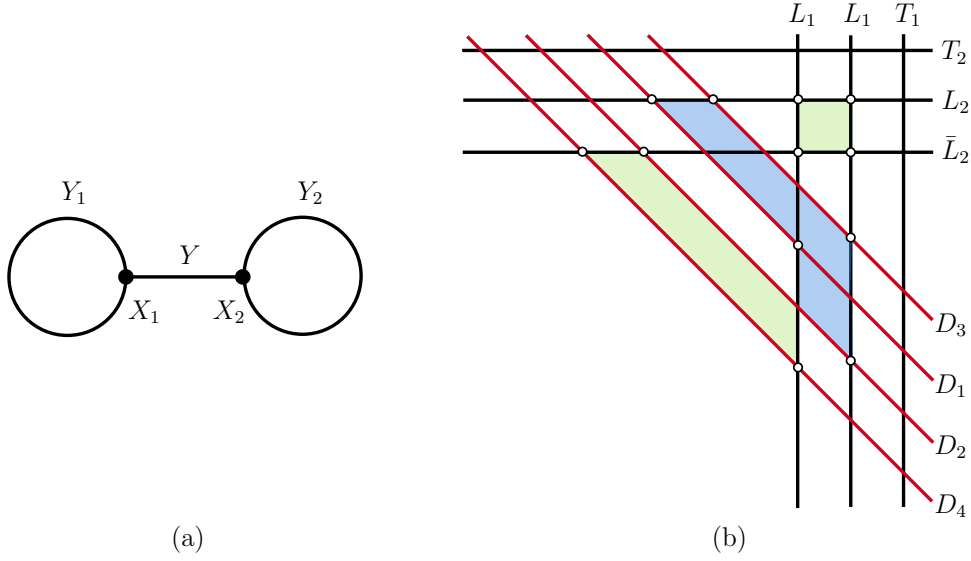


**Figure 7.** (a). The diagram for two-site two-tadpole dumbbell wavefunction coefficient where the late-time boundary and external legs are omitted. (b). The hyperplane arrangement of dumbbell system in the configuration  $X \gg Y$ <sup>5</sup> where all non-vanishing codimension-2 boundaries of  $\bar{\Omega}_{\mathcal{P}_{\text{dbl}}}$  are marked as the white intersection points, allowing us to extract the triangulation corresponding to the tree factorization. The triangulation yields a net contribution by summing over all triangular areas achieved through the matching of residues on codimension-2 boundaries. The net contribution corresponds to the colored regions, with blue areas assigned a weight of +1 and green areas a weight of -1. Summing the forms associated with colored regions, weighted accordingly, reproduces  $\bar{\Omega}_{\mathcal{P}_{\text{dbl}}}$ .

where each form corresponds to a triangular region as enclosed by the three hyperplanes appearing in the denominator of its expression. Further, we can define the canonical 2-form associated with the two-site tree-level parent function  $\bar{\Omega}_{\mathcal{P}_{\text{tree}}}$  as:

$$\bar{\Omega}_{\mathcal{P}_{\text{tree}}} \equiv \frac{-2Y}{(x_1 + x_2 + X_1 + X_2)(x_1 + X_1 + Y)(x_2 + X_2 + Y)}. \quad (5.12)$$

Hence, each canonical form  $\bar{\Omega}_{\mathcal{P}_i}$  can be interpreted as a shifted version of  $\bar{\Omega}_{\mathcal{P}_{\text{tree}}}$ :

$$\begin{aligned} \bar{\Omega}_{\mathcal{P}_1} &= \bar{\Omega}_{\mathcal{P}_{\text{tree}}} \Big|_{X_1 \rightarrow X_1 + 2Y_1}, & \bar{\Omega}_{\mathcal{P}_2} &= \bar{\Omega}_{\mathcal{P}_{\text{tree}}} \Big|_{X_2 \rightarrow X_2 + 2Y_2}, \\ \bar{\Omega}_{\mathcal{P}_3} &= \bar{\Omega}_{\mathcal{P}_{\text{tree}}}, & \bar{\Omega}_{\mathcal{P}_4} &= \bar{\Omega}_{\mathcal{P}_{\text{tree}}} \Big|_{\substack{X_1 \rightarrow X_1 + 2Y_1 \\ X_2 \rightarrow X_2 + 2Y_2}}. \end{aligned} \quad (5.13)$$

Now, inspecting Eq. (5.11) or Eq. (5.13), it becomes evident that each  $\mathcal{P}_i$  is associated with a distinct  $L$ -pair as its codimension-2 singularity. This distinction validates these functions as top-layer components within the preferred triangular basis. In essence, the four parent functions cannot be merged into a single entity because the corresponding letters, arising from their respective shifts, are inherently different. Specifically, the differential equation for each parent function takes the form:

$$d\mathcal{P}_i = \varepsilon [\mathcal{P}_i (l_{1,i} + l_{2,i}) + \dots], \quad (5.14)$$

<sup>5</sup>This configuration is chosen for convenience so that one does not need to deal with the relative position between  $L$  and  $D$  planes.

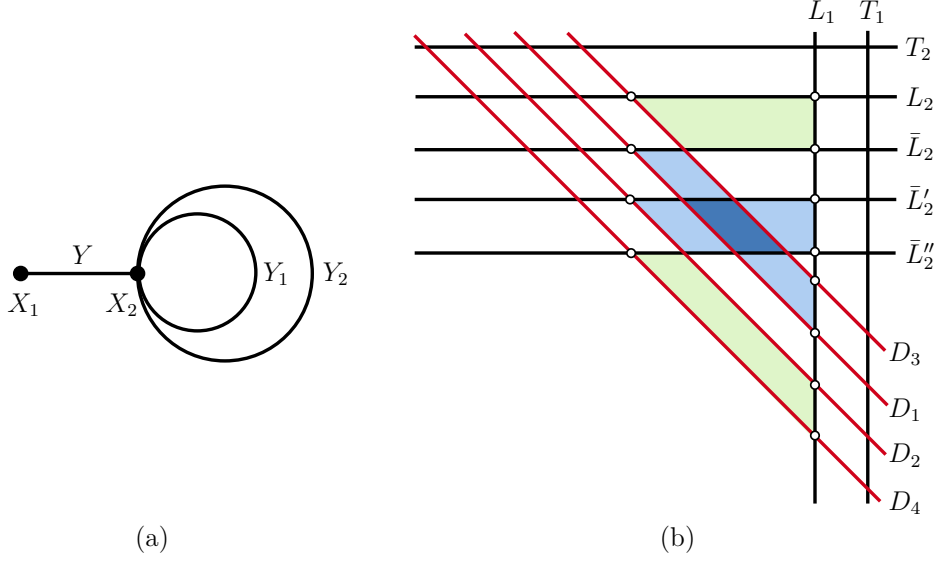


**Figure 8.** (a). The diagram for two-site two-tadpole lollipop wavefunction coefficient. (b). The corresponding hyperplane arrangement in the configuration  $X \gg Y$ . The net contribution is corresponding to the colored regions, with dark blue area assigned a weight of  $+2$ , blue areas  $+1$  and green areas  $-1$ . Summing the forms associated with the weighted regions reproduces  $\bar{\Omega}_{\mathcal{P}_{\text{lollipop}}}$ .

where  $\{\mathcal{P}_i\}$ ,  $\{l_{1,i}\}$  and  $\{l_{2,i}\}$  (with  $i=1, \dots, 4$ ) are the tree parent functions and the letters originating from the shifts (5.13). Within this framework, each shifted tree system appears as an integrable  $4 \times 4$  tree block in the matrix  $\tilde{A}$ , simplifying its structure significantly. From the perspective of the preferred triangle basis, it is clear that the entire system, consisting of 24 bounded regions, is spanned by 4 P-functions, 16 F-functions and 4 Q-functions, while the two-loop dumbbell system utilizes only 8 of these 16 F-functions.

**Lollipop** Another example with a similar tree-level factorization is a diagram representing a two-tadpole lollipop with a central ring, as illustrated in Fig. 8(a). The corresponding wavefunction coefficient is given by

$$\begin{aligned} \psi_{(2,2)}^{\text{lollipop}} &= 8YY_1Y_2 \int \frac{d\mu}{L_1 \bar{L}_2' D_3} \left( \frac{1}{L_2 \bar{L}_2} + \frac{1}{L_2 \bar{L}_2'} + \frac{1}{\bar{L}_2 D_1} + \frac{1}{\bar{L}_2' D_2} + \frac{1}{D_1 D_4} + \frac{1}{D_2 D_4} \right) \\ &\equiv \int d\mu \bar{\Omega}_{\mathcal{P}_{\text{lollipop}}}, \end{aligned} \quad (5.15)$$

where the hyperplanes are defined as follows:

$$\begin{aligned} L_1 &= x_1 + X_1 + Y, & L_2 &= x_2 + X_2 + Y, & \bar{L}_2 &= x_2 + X_2 + Y + 2Y_1, \\ \bar{L}_2' &= x_2 + X_2 + Y + 2Y_2, & \bar{L}_2'' &= x_2 + X_2 + Y + 2(Y_1 + Y_2), \\ D_1 &= x_1 + x_2 + X_1 + X_2 + 2Y_1, & D_2 &= x_1 + x_2 + X_1 + X_2 + 2Y_2, \\ D_3 &= x_1 + x_2 + X_1 + X_2, & D_4 &= x_1 + x_2 + X_1 + X_2 + 2(Y_1 + Y_2). \end{aligned} \quad (5.16)$$

A similar analysis in the hyperplane arrangement [cf. Fig. 8(b)] shows that the tree factorization for  $\bar{\Omega}_{\mathcal{P}_{\text{lollipop}}}$  is given by

$$\bar{\Omega}_{\mathcal{P}_{\text{lollipop}}} = \bar{\Omega}_{\mathcal{P}_1} + \bar{\Omega}_{\mathcal{P}_2} - \bar{\Omega}_{\mathcal{P}_3} - \bar{\Omega}_{\mathcal{P}_4}, \quad (5.17)$$



where  $\bar{\Omega}_{\mathcal{P}_i}$  can be expressed in terms of Eq. (5.16) as follows:

$$\bar{\Omega}_{\mathcal{P}_1} = \frac{-2Y}{L_1 \bar{L}_2 D_1}, \quad \bar{\Omega}_{\mathcal{P}_2} = \frac{-2Y}{L_1 \bar{L}'_2 D_2}, \quad \bar{\Omega}_{\mathcal{P}_3} = \frac{-2Y}{L_1 L_2 D_3}, \quad \bar{\Omega}_{\mathcal{P}_4} = \frac{-2Y}{L_1 \bar{L}''_2 D_4}, \quad (5.18)$$

which each form corresponds to a triangular region as enclosed by the three hyperplanes. Further, each  $\bar{\Omega}_{\mathcal{P}_i}$  can be regarded as a shifted version of Eq. (5.12):

$$\begin{aligned} \bar{\Omega}_{\mathcal{P}_1} &= \bar{\Omega}_{\mathcal{P}_{\text{tree}}} \Big|_{X_2 \rightarrow X_2 + 2Y_1}, & \bar{\Omega}_{\mathcal{P}_2} &= \bar{\Omega}_{\mathcal{P}_{\text{tree}}} \Big|_{X_2 \rightarrow X_2 + 2Y_2}, \\ \bar{\Omega}_{\mathcal{P}_3} &= \bar{\Omega}_{\mathcal{P}_{\text{tree}}}, & \bar{\Omega}_{\mathcal{P}_4} &= \bar{\Omega}_{\mathcal{P}_{\text{tree}}} \Big|_{X_2 \rightarrow X_2 + 2(Y_1 + Y_2)}. \end{aligned} \quad (5.19)$$

Inspecting Eq. (5.18) or Eq. (5.19), each  $\mathcal{P}_i$  has a distinct  $L$ -pair, serving as valid top-layer basis. Similar to the dumbbell case, the relevant  $\tilde{A}$  has four  $4 \times 4$  blocks. The whole system in the preferred basis contains 4 P-functions, 20 F-functions and 4 Q-functions, corresponding to a total of 28 bounded regions, while the two-loop lollipop system only involves 8 of these 20 F-functions.

**Gourd** The final example of a two-site, two-loop topology is the one-tadpole gourd diagram shown in Fig. 9(a), which exhibits a mixed structure combining features of both bubble and tadpole systems. Its wavefunction coefficient is derived as:

$$\begin{aligned} \psi_{(2,2)}^{\text{grd}} &= 8Y_1 Y_2 Y_3 \int \frac{d\mu}{L_1 \bar{L}_2 D_3} \left[ \frac{1}{L_2} \left( \frac{1}{D_1} + \frac{1}{D_2} \right) + \frac{1}{\bar{D}_1} \left( \frac{1}{D_1} + \frac{1}{\bar{D}_3} \right) + \frac{1}{\bar{D}_2} \left( \frac{1}{D_2} + \frac{1}{\bar{D}_3} \right) \right] \\ &\equiv \int d\mu \bar{\Omega}_{\mathcal{P}_{\text{grd}}}, \end{aligned} \quad (5.20)$$

where the hyperplanes are defined as follows:

$$\begin{aligned} L_1 &= x_1 + X_1 + Y_1 + Y_2, & \bar{L}_2 &= x_2 + X_2 + Y_1 + Y_2 + 2Y_3, \\ L_2 &= x_2 + X_2 + Y_1 + Y_2, & \bar{D}_1 &= x_1 + x_2 + X_1 + X_2 + 2(Y_1 + Y_3), \\ D_1 &= x_1 + x_2 + X_1 + X_2 + 2Y_1, & \bar{D}_2 &= x_1 + x_2 + X_1 + X_2 + 2(Y_2 + Y_3), \\ D_2 &= x_1 + x_2 + X_1 + X_2 + 2Y_2, & \bar{D}_3 &= x_1 + x_2 + X_1 + X_2 + 2Y_3. \end{aligned} \quad (5.21)$$

Inspecting Fig. 9(b) and evaluating each residue on codimension-2 boundaries associated with  $\mathcal{P}_{\text{grd}}$ , we find that tree factorization for  $\bar{\Omega}_{\mathcal{P}_{\text{grd}}}$  is

$$\bar{\Omega}_{\mathcal{P}_{\text{grd}}} = \bar{\Omega}_{\mathcal{P}_1} + \bar{\Omega}_{\mathcal{P}_2} - \bar{\Omega}_{\mathcal{P}_3} - (\bar{\Omega}_{\mathcal{P}'_1} + \bar{\Omega}_{\mathcal{P}'_2} - \bar{\Omega}_{\mathcal{P}'_3}), \quad (5.22)$$

where in terms of Eq. (5.21),  $\bar{\Omega}_{\mathcal{P}_i}, \bar{\Omega}_{\mathcal{P}'_i}$  can be further expressed as follows:

$$\bar{\Omega}_{\mathcal{P}_1} = \frac{-2Y_2}{L_1 L_2 D_1}, \quad \bar{\Omega}_{\mathcal{P}_2} = \frac{-2Y_1}{L_1 L_2 D_2}, \quad \bar{\Omega}_{\mathcal{P}_3} = \frac{-2(Y_1 + Y_2)}{L_1 L_2 D_3}, \quad (5.23a)$$

$$\bar{\Omega}_{\mathcal{P}'_1} = \frac{-2Y_2}{L_1 \bar{L}_2 \bar{D}_1}, \quad \bar{\Omega}_{\mathcal{P}'_2} = \frac{-2Y_1}{L_1 \bar{L}_2 \bar{D}_2}, \quad \bar{\Omega}_{\mathcal{P}'_3} = \frac{-2(Y_1 + Y_2)}{L_1 \bar{L}_2 \bar{D}_3}. \quad (5.23b)$$

Similarly, each  $\bar{\Omega}_{\mathcal{P}_i}$  and  $\bar{\Omega}_{\mathcal{P}'_i}$  is represented as a shifted version of Eq. (5.12):

$$\bar{\Omega}_{\mathcal{P}_1} = \bar{\Omega}_{\mathcal{P}_{\text{tree}}} \Big|_{\substack{X_1 \rightarrow X_1 + Y_1 \\ X_2 \rightarrow X_2 + Y_1 \\ Y_2 \rightarrow Y_2}}, \quad \bar{\Omega}_{\mathcal{P}'_1} = \bar{\Omega}_{\mathcal{P}_{\text{tree}}} \Big|_{\substack{X_1 \rightarrow X_1 + Y_1 \\ X_2 \rightarrow X_2 + Y_1 + 2Y_3 \\ Y_2 \rightarrow Y_2}},$$

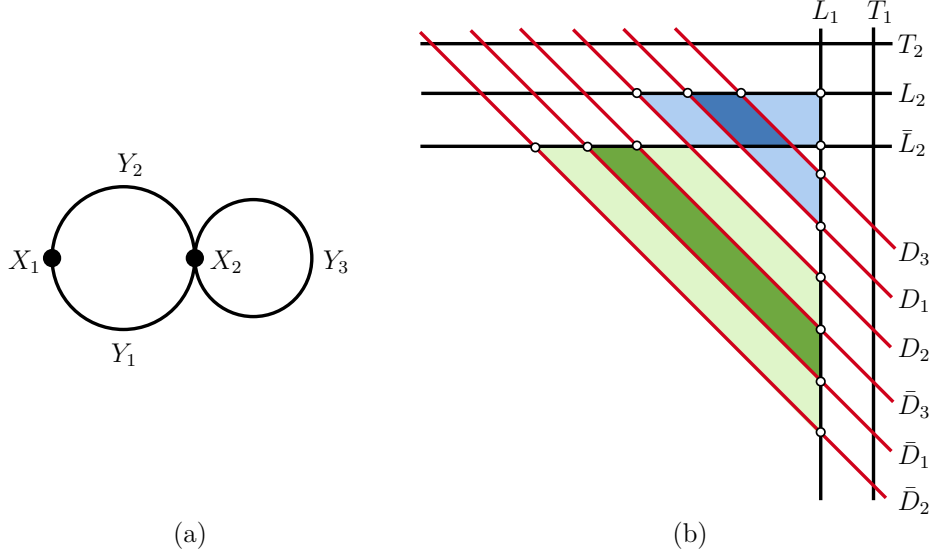


**Figure 9.** (a). The diagram for a two-site two-loop topology with one bubble and one tadpole wavefunction coefficient. (b). The corresponding hyperplane arrangement where the net contribution is corresponding to the colored regions, with dark blue area assigned a weight of +2, blue areas +1 and green areas -1. Summing the forms associated with the weighted regions reproduces  $\bar{\Omega}_{\mathcal{P}_{\text{grd}}}$ .

$$\begin{aligned}
\bar{\Omega}_{\mathcal{P}_2} &= \bar{\Omega}_{\mathcal{P}_{\text{tree}}} \Big|_{\substack{X_1 \rightarrow X_1 + Y_2 \\ X_2 \rightarrow X_2 + Y_2 \\ Y \rightarrow Y_1}}, & \bar{\Omega}_{\mathcal{P}'_2} &= \bar{\Omega}_{\mathcal{P}_{\text{tree}}} \Big|_{\substack{X_1 \rightarrow X_1 + Y_2 \\ X_2 \rightarrow X_2 + Y_2 + 2Y_3 \\ Y \rightarrow Y_1}}, \\
\bar{\Omega}_{\mathcal{P}_3} &= \bar{\Omega}_{\mathcal{P}_{\text{tree}}} \Big|_{Y \rightarrow Y_1 + Y_2}, & \bar{\Omega}_{\mathcal{P}'_3} &= \bar{\Omega}_{\mathcal{P}_{\text{tree}}} \Big|_{X_2 \rightarrow X_2 + 2Y_3, Y \rightarrow Y_1 + Y_2}.
\end{aligned} \tag{5.24}$$

At this stage, all  $\mathcal{P}_i$  share the same  $(L_1, L_2)$ -pair, while  $\mathcal{P}'_i$  share the same  $(L_1, L'_2)$ -pair. This observation suggests that the six parent functions can be merged into just two parent functions. And they can be grouped into a one-loop bubble and a shifted one-loop bubble:

$$\bar{\Omega}_{\mathcal{P}_1} + \bar{\Omega}_{\mathcal{P}_2} - \bar{\Omega}_{\mathcal{P}_3} = \bar{\Omega}_{\mathcal{P}_{\text{bub}}}, \quad \bar{\Omega}_{\mathcal{P}'_1} + \bar{\Omega}_{\mathcal{P}'_2} - \bar{\Omega}_{\mathcal{P}'_3} = \bar{\Omega}_{\mathcal{P}_{\text{bub}}} \Big|_{X_2 \rightarrow X_2 + 2Y_3}, \tag{5.25}$$

where  $\bar{\Omega}_{\mathcal{P}_{\text{bub}}}$  is defined in Eq. (3.10). Hence, the matrix  $\tilde{A}^{\text{grd}}$  takes a block-diagonal form:

$$\tilde{A}_{20 \times 20}^{\text{grd}} = \tilde{A}_{10 \times 10}^{\text{bub}} \oplus \tilde{A}_{10 \times 10}^{\text{bub}} \Big|_{X_2 \rightarrow X_2 + 2Y_3}, \tag{5.26}$$

where  $\tilde{A}_{10 \times 10}^{\text{bub}}$  is defined in Eq. (3.30). This can be further diagonalized into two  $4 \times 4$  plus four  $3 \times 3$  blocks by choosing either one of  $\mathcal{P}_i$  and one of  $\mathcal{P}'_i$  as the two top-layer functions in the preferred triangle basis. The whole system in the preferred basis has 2 P-functions, 18 F-functions, and 6 Q-functions corresponding to a total of 26 bounded regions, while the two-loop gourd system selectively involves 12 of these 18 F-functions.

Finally, for a two-site arbitrary loop diagram, its building blocks consist of a unshifted bubble-type (including tree) diagram and all the shifted bubbles induced by the internal lines of all tadpole loops. For instance, in the case of gourd diagram, its building blocks are the unshifted bubble at left and a shifted bubble determined by the tadpole loop on the right. Since the vertex  $X_2$  is connected to the tadpole, the resulting shift for the bubble

is given by  $X_2 \rightarrow X_2 + 2Y_3$ . And the final result is obtained by combining the unshifted bubble with the shifted bubbles [cf. Eqs. (5.22), (5.25)]. Pictorially, for the three examples discussed in this section, we can mark the corresponding tadpole internal lines with either a red or hollow cross sign. By following the rules outlined in Section 4.2, the corresponding family trees can be generated, from which the associated differential equations can be derived. The specific details of this procedure will not be elaborated further in this paper. The specific details of this procedure will be elaborated in this our future work.

## 6 Conclusion and Outlook

In this study, we have systematically derived the canonical differential equations governing the wavefunction coefficients for bubble and tadpole configurations in power-law FRW cosmology, extending the kinematic flow method to higher-loop scenarios. By employing the tools of relative twisted cohomology and hyperplane arrangements, we constructed a unified framework for analyzing integral families, from which we obtained the associated canonical differential equations. This framework not only simplifies the calculation process but also introduces a systematic approach to two-site higher-loop calculations, marking a significant advance in the application of the kinematic flow method beyond the tree-level systems [7, 8].

Further, our analysis provides several key insights into the underlying structures of cosmological correlators. First, we have found that tadpole systems exhibit a broader set of parent functions due to the existence of distinct, non-overlapping relative hyperplanes of each parent function. This contrasts with tree and bubble diagrams, where a single parent function is found. Second, we demonstrated that the wavefunction coefficients for tadpole configurations selectively probe only a subset of the full vector space. Despite the apparent higher-dimensional structure suggested by the hyperplane arrangements, the coefficients engage with a reduced section of the space. Third, we showed that the differential equations governing these systems can be efficiently derived from family trees generated through the evolution of marked tubes. Finally, our approach provides deep insights and robust methods for obtaining the differential equations at even higher-loop orders for the first time. Specifically, the building blocks consist of a unshifted bubble-type diagram combined with all possible shifts induced by tadpoles. The corresponding graphical representation of these evolution processes not only facilitates the computation of complex integrals but also provides deeper insight into the geometric and topological features of cosmological wavefunction coefficients.

As we look to the future, our research will focus on extending these methodologies to higher-loop configurations with more sites and exploring massive correlators. Additionally, the study of massive scalar fields presents an even more intriguing avenue of exploration. In Ref. [23], the differential equations for two-site tree-level wavefunction coefficients in dS spacetime were analyzed. Incorporating an extra mass term  $-\sqrt{g}m^2\phi^2/2$  into Eq. (2.1) complicates the equation of motion for the scalar field, leading to solutions involving the second kind Hankel function  $H_v^{(2)}(-E\eta)$  with  $v = \sqrt{1-4m^2}/2$  [4]. Hence, it will results in a more intricate hyperplane configuration. For instance, in the two-site tree-level case,

there are four twist variables  $\{x_1, x_2, t_1, t_2\}$ . Despite these complexities, the hyperplane arrangements and kinematic flow for both massive tree-level and loop-level scenarios remain a compelling area for further investigation.

## Acknowledgments

We are grateful to Paolo Benincasa, Giacomo Brunello, J. J. Carrasco, Zong-Zhe Du, Jianyu Gong, Xu Wang and Yu Wu for their insightful discussions and valuable suggestions. YH and CS would like to acknowledge the Northwestern University Amplitudes and Insight group, Department of Physics and Astronomy, and Weinberg College for support.

## A The Derivation of Two-Site One-Loop DEs from IBP

In this appendix, we provide additional details on the derivation of the differential equations for certain functions that were omitted in the main text.

### A.1 Two-Site One-Loop Bubble

In Eq. (3.5) of Section 3.1,  $\mathbf{F}_3 = \{\mathcal{P}_3, \mathcal{F}_3, \tilde{\mathcal{F}}_3, \mathcal{Q}_3\}$  and the total derivative for  $\mathbf{F}_3$  is

$$d\mathbf{F}_3 = \partial_{X_1} \mathbf{F}_3 dX_1 + \partial_{X_2} \mathbf{F}_3 dX_2 + \partial_{Y_1} \mathbf{F}_3 dY_1 + \partial_{Y_2} \mathbf{F}_3 dY_2. \quad (\text{A.1})$$

The differentiation of external energy  $X_1$  with respect to the parent function  $\mathcal{P}_3$  can be calculated as follows:

$$\begin{aligned} \partial_{X_1} \mathcal{P}_3 &= \int d\mu \partial_{x_1} \bar{\Omega}_{\mathcal{P}_3} = \varepsilon \int d\mu \left( -\frac{\bar{\Omega}_{\mathcal{P}_3}}{T_1} \right) \\ &= \varepsilon \int d\mu \left\{ \left( \text{Res} \left[ \frac{-\bar{\Omega}_{\mathcal{P}_3}}{T_1} \right]_{\substack{L_1=0 \\ L_2=0}}, \text{Res} \left[ \frac{-\bar{\Omega}_{\mathcal{P}_3}}{T_1} \right]_{\substack{T_1=0 \\ L_2=0}} \right) (\bar{\Omega}_{\mathcal{P}_3}, \bar{\Omega}_{\mathcal{F}_3})^T \right\} \\ &= -\varepsilon \int d\mu \left[ \frac{1}{X_1 + Y_1 + Y_2} \bar{\Omega}_{\mathcal{P}_3} + \frac{2(Y_1 + Y_2)}{(X_1 - Y_1 - Y_2)(X_1 + Y_1 + Y_2)} \bar{\Omega}_{\mathcal{F}_3} \right] \\ &= -\varepsilon \left[ \frac{1}{X_1 + Y_1 + Y_2} \mathcal{P}_3 + \left( \frac{1}{X_1 - Y_1 - Y_2} - \frac{1}{X_1 + Y_1 + Y_2} \right) \mathcal{F}_3 \right]. \end{aligned} \quad (\text{A.2})$$

Similarly, the differentiation with respect to  $X_2$  follows the same steps as for  $X_1$ , we only need to make the following substitutions:  $X_1 \rightarrow X_2$  and  $\mathcal{F}_3 \rightarrow \tilde{\mathcal{F}}_3$  in Eq. (A.2):

$$\partial_{X_2} \mathcal{P}_3 = \varepsilon \left[ \frac{1}{X_2 + Y_1 + Y_2} \mathcal{P}_3 + \left( \frac{1}{X_2 - Y_1 - Y_2} - \frac{1}{X_2 + Y_1 + Y_2} \right) \tilde{\mathcal{F}}_3 \right]. \quad (\text{A.3})$$

The differentiation of internal energy  $Y_1$  with respect to  $\mathcal{P}_3$  can be computed as follows:

$$\begin{aligned} \partial_{Y_1} \mathcal{P}_3 &= \int d\mu \left[ \partial_{x_1} \left( \frac{-x_1 - X_1}{Y_1 + Y_2} \bar{\Omega}_{\mathcal{P}_3} \right) + \partial_{x_2} \left( \frac{-x_2 - X_2}{Y_1 + Y_2} \bar{\Omega}_{\mathcal{P}_3} \right) \right] \\ &= \varepsilon \int d\mu \left\{ \left( \text{Res} \left[ \frac{(x_1 + X_1) \bar{\Omega}_{\mathcal{P}_3}}{T_1(Y_1 + Y_2)} \right]_{\substack{L_1=0 \\ L_2=0}}, \text{Res} \left[ \frac{(x_1 + X_1) \bar{\Omega}_{\mathcal{P}_3}}{T_1(Y_1 + Y_2)} \right]_{\substack{T_1=0 \\ L_2=0}} \right) (\bar{\Omega}_{\mathcal{P}_3}, \bar{\Omega}_{\mathcal{F}_3})^T \right\} \end{aligned}$$

$$\begin{aligned}
& + \left( \text{Res} \left[ \frac{(x_1+X_1)\bar{\Omega}_{\mathcal{P}_3}}{T_2(Y_1+Y_2)} \right]_{L_2=0}^{L_1=0}, \text{Res} \left[ \frac{(x_1+X_1)\bar{\Omega}_{\mathcal{P}_3}}{T_2(Y_1+Y_2)} \right]_{L_1=0}^{T_2=0} \right) (\bar{\Omega}_{\mathcal{P}_3}, \bar{\Omega}_{\tilde{\mathcal{F}}_3})^T \Big\} \\
= & \varepsilon \left[ \left( \frac{1}{X_1+Y_1+Y_2} + \frac{1}{X_2+Y_1+Y_2} \right) \mathcal{P}_3 - \left( \frac{1}{X_1+Y_1+Y_2} + \frac{1}{X_1-Y_1-Y_2} \right) \mathcal{F}_3 \right. \\
& \left. - \left( \frac{1}{X_2+Y_1+Y_2} + \frac{1}{X_2-Y_1-Y_2} \right) \tilde{\mathcal{F}}_3 \right]. \tag{A.4}
\end{aligned}$$

By replacing  $Y_1 \rightarrow Y_2$  in Eq. (A.4), it is not difficult to derive the result for  $Y_2$ :

$$\begin{aligned}
\partial_{Y_2} \mathcal{P}_3 = & \varepsilon \left[ \left( \frac{1}{X_1+Y_1+Y_2} + \frac{1}{X_2+Y_1+Y_2} \right) \mathcal{P}_3 - \left( \frac{1}{X_1+Y_1+Y_2} + \frac{1}{X_1-Y_1-Y_2} \right) \mathcal{F}_3 \right. \\
& \left. - \left( \frac{1}{X_2+Y_1+Y_2} + \frac{1}{X_2-Y_1-Y_2} \right) \tilde{\mathcal{F}}_3 \right] = \partial_{Y_1} \mathcal{P}_3. \tag{A.5}
\end{aligned}$$

Thus, in terms of the total derivative (A.1) and writing in dlog forms, we finally obtain the full differential equation for  $\mathcal{P}_3$ :

$$\begin{aligned}
d\mathcal{P}_3 = & -\varepsilon \left[ (\mathcal{P}_3 - \mathcal{F}_3) d\log(X_1+Y_1+Y_2) + (\mathcal{P}_3 - \tilde{\mathcal{F}}_3) d\log(X_2+Y_1+Y_2) \right. \\
& \left. + \mathcal{F}_3 d\log(X_1-Y_1-Y_2) + \tilde{\mathcal{F}}_3 d\log(X_2-Y_1-Y_2) \right]. \tag{A.6}
\end{aligned}$$

Next, we examine the differentiation of the decedent functions  $\mathcal{F}_3$  and  $\tilde{\mathcal{F}}_3$ . For  $\mathcal{F}_3$ , the results with respect to the external energies is given by

$$\begin{aligned}
\partial_{X_1} \mathcal{F}_3 = & \int d\mu \left[ \partial_{x_1} \left( \frac{-T_1}{X_1-Y_1-Y_2} \bar{\Omega}_{\mathcal{F}_3} \right) + \partial_{x_2} \left( \frac{-L_2}{X_1-Y_1-Y_2} \bar{\Omega}_{\mathcal{F}_3} \right) \right] \\
= & \varepsilon \int d\mu \left\{ \left( \text{Res} \left[ \frac{\bar{\Omega}_{\mathcal{F}_3}}{X_1-Y_1-Y_2} \right]_{L_2=0}^{T_1=0}, \text{Res} \left[ \frac{\bar{\Omega}_{\mathcal{F}_3}}{X_1-Y_1-Y_2} \right]_{T_2=0}^{T_1=0} \right) (\bar{\Omega}_{\mathcal{F}_3}, \bar{\Omega}_{\mathcal{Q}_3})^T \right. \\
& \left. + \left( \text{Res} \left[ \frac{L_2 \bar{\Omega}_{\mathcal{F}_3}}{T_2(X_1-Y_1-Y_2)} \right]_{L_2=0}^{T_1=0}, \text{Res} \left[ \frac{L_2 \bar{\Omega}_{\mathcal{F}_3}}{T_2(X_1-Y_1-Y_2)} \right]_{T_2=0}^{T_1=0} \right) (\bar{\Omega}_{\mathcal{F}_3}, \bar{\Omega}_{\mathcal{Q}_3})^T \right\} \\
= & \varepsilon \left[ \frac{1}{X_1-Y_1-Y_2} \mathcal{F}_3 + \frac{1}{X_1+X_2} \mathcal{Q}_3 \right], \tag{A.7a}
\end{aligned}$$

$$\partial_{X_2} \mathcal{F}_3 = \int d\mu \partial_{x_2} \bar{\Omega}_{\mathcal{F}_3} \tag{A.7b}$$

$$= \varepsilon \left[ \frac{1}{X_2+Y_1+Y_2} \mathcal{F}_3 + \left( \frac{1}{X_1+X_2} - \frac{1}{X_2+Y_1+Y_2} \right) \mathcal{Q}_3 \right], \tag{A.7c}$$

and the differentiation with respect to the internal energies is computed as:

$$\begin{aligned}
\partial_{Y_1} \mathcal{F}_3 = & \int d\mu \left[ \partial_{x_1} \left( \frac{x_1}{X_1-Y_1-Y_2} \bar{\Omega}_{\mathcal{F}_3} \right) + \partial_{x_2} \left( \frac{x_2+X_1+X_2}{X_1-Y_1-Y_2} \bar{\Omega}_{\mathcal{F}_3} \right) \right] \\
= & \varepsilon \left[ \left( -\frac{1}{X_1-Y_1-Y_2} + \frac{1}{X_2+Y_1+Y_2} \right) \mathcal{F}_3 - \frac{1}{X_2+Y_1+Y_2} \mathcal{Q}_3 \right], \tag{A.8a}
\end{aligned}$$

$$\partial_{Y_2} \mathcal{F}_3 = \partial_{Y_1} \mathcal{F}_3. \tag{A.8b}$$

We omit the derivation for  $\tilde{\mathcal{F}}_3$ . In terms of the total derivative, the complete canonical differential equations for  $\mathcal{F}_3$  and  $\tilde{\mathcal{F}}_3$  are obtained as:

$$d\mathcal{F}_3 = \varepsilon [\mathcal{F}_3 d\log(X_1 - Y_1 - Y_2) + (\mathcal{F}_3 - \mathcal{Q}_3) d\log(X_2 + Y_1 + Y_2) + \mathcal{Q}_3 d\log(X_1 + X_2)], \quad (\text{A.9a})$$

$$d\tilde{\mathcal{F}}_3 = \varepsilon [\tilde{\mathcal{F}}_3 d\log(X_2 - Y_1 - Y_2) + (\tilde{\mathcal{F}}_3 - \mathcal{Q}_3) d\log(X_1 + Y_1 + Y_2) + \mathcal{Q}_3 d\log(X_1 + X_2)]. \quad (\text{A.9b})$$

Finally, for the descendant function  $\mathcal{Q}_3$ , we can derive

$$\begin{aligned} \partial_{X_1} \mathcal{Q}_3 &= \int d\mu \left[ \partial_{x_1} \left( \frac{-x_1}{X_1 + X_2} \bar{\Omega}_{\mathcal{Q}_3} \right) + \partial_{x_2} \left( \frac{-x_2}{X_1 + X_2} \bar{\Omega}_{\mathcal{Q}_3} \right) \right] \\ &= 2\varepsilon \int d\mu \operatorname{Res} \left[ \frac{\bar{\Omega}_{\mathcal{Q}_3}}{X_1 - X_2} \right]_{\substack{T_1=0 \\ T_2=0}} \bar{\Omega}_{\mathcal{Q}_3} = 2\varepsilon \frac{\mathcal{Q}_3}{X_1 + X_2}, \end{aligned} \quad (\text{A.10a})$$

$$\partial_{X_2} \mathcal{Q}_3 = \partial_{X_1} \mathcal{Q}_3, \quad (\text{A.10b})$$

$$\partial_{Y_1} \mathcal{Q}_3 = \partial_{Y_2} \mathcal{Q}_3 = 0, \quad (\text{A.10c})$$

where the differential equation for  $\mathcal{Q}_3$  is obtained as:

$$d\mathcal{Q}_3 = 2\varepsilon \mathcal{Q}_3 d\log(X_1 + X_2). \quad (\text{A.11})$$

## A.2 Two-Site One-Loop Tadpole

The definitions for  $\mathcal{F}_2^u$  and  $\mathcal{F}_3^u$  can be found in (3.45b) of Section 3.2. The differentiation for the function  $\mathcal{F}_2^u$  with respect to the external and internal energies is computed as:

$$\begin{aligned} \partial_{X_1} \mathcal{F}_2^u &= \int d\mu \left[ \partial_{x_1} \left( \frac{-x_1}{X_1 - Y_1 + 2Y_2} \bar{\Omega}_{\mathcal{F}_2^u} \right) + \partial_{x_2} \left( \frac{-L_2}{X_1 - Y_1 + 2Y_2} \bar{\Omega}_{\mathcal{F}_2^u} \right) \right] \\ &= \varepsilon \left[ \frac{1}{X_1 - Y_1 + 2Y_2} \mathcal{F}_2^u + \frac{1}{X_1 + X_2 + 2Y_2} \mathcal{Q}_2 \right], \end{aligned} \quad (\text{A.12a})$$

$$\partial_{X_2} \mathcal{F}_2^u = \int d\mu \partial_{x_2} \bar{\Omega}_{\mathcal{F}_2^u} = \varepsilon \left[ \frac{1}{X_2 + Y_1} \mathcal{F}_2^u + \left( \frac{1}{X_1 + X_2 + 2Y_2} - \frac{1}{X_2 + Y_1} \right) \mathcal{Q}_2 \right], \quad (\text{A.12b})$$

$$\begin{aligned} \partial_{Y_1} \mathcal{F}_2^u &= \int d\mu \left[ \partial_{x_1} \left( \frac{x_1}{X_1 - Y_1 + 2Y_2} \bar{\Omega}_{\mathcal{F}_2^u} \right) + \partial_{x_2} \left( \frac{x_2 + X_1 + X_2 + 2Y_2}{X_1 - Y_1 + 2Y_2} \bar{\Omega}_{\mathcal{F}_2^u} \right) \right] \\ &= \varepsilon \left[ \left( \frac{1}{X_2 + Y_1} - \frac{1}{X_1 - Y_1 + 2Y_2} \right) \mathcal{F}_2^u - \frac{1}{X_2 + Y_1} \mathcal{Q}_2 \right], \end{aligned} \quad (\text{A.12c})$$

$$\begin{aligned} \partial_{Y_2} \mathcal{F}_2^u &= \int d\mu \left[ \partial_{x_1} \left( \frac{-2x_1}{X_1 - Y_1 + 2Y_2} \bar{\Omega}_{\mathcal{F}_2^u} \right) + \partial_{x_2} \left( \frac{-2L_2}{X_1 - Y_1 + 2Y_2} \bar{\Omega}_{\mathcal{F}_2^u} \right) \right] \\ &= \varepsilon \left[ \frac{2}{X_1 - Y_1 + 2Y_2} \mathcal{F}_2^u + \frac{2}{X_1 + X_2 + 2Y_2} \mathcal{Q}_2 \right]. \end{aligned} \quad (\text{A.12d})$$

Collectively, the canonical differential equation for  $\mathcal{F}_2^u$  is

$$\begin{aligned} d\mathcal{F}_2^u &= \varepsilon [\mathcal{F}_2^u d\log(X_1 - Y_1 + 2Y_2) + (\mathcal{F}_2^u - \mathcal{Q}_2) d\log(X_2 + Y_1) \\ &\quad + \mathcal{Q}_2 d\log(X_1 + X_2 + 2Y_2)]. \end{aligned} \quad (\text{A.13})$$

The differentiation for the function  $\mathcal{F}_3^u$  with respect to the external and internal energies is computed as:

$$\partial_{X_1} \mathcal{F}_3^u = \int d\mu \left[ \partial_{x_1} \left( \frac{-x_1}{X_1 - Y_1 - 2Y_2} \bar{\Omega}_{\mathcal{F}_3^u} \right) + \partial_{x_2} \left( \frac{-x_2 - X_2 - Y_1 - 2Y_2}{X_1 - Y_1 - 2Y_2} \bar{\Omega}_{\mathcal{F}_3^u} \right) \right]$$

$$= \varepsilon \left[ \frac{1}{X_1 - Y_1 - 2Y_2} \bar{\Omega}_{\mathcal{F}_3^u} + \frac{1}{X_1 + X_2} \bar{\Omega}_{\mathcal{Q}_3} \right], \quad (\text{A.14a})$$

$$\begin{aligned} \partial_{X_2} \mathcal{F}_3^u &= \int d\mu \partial_{x_2} \bar{\Omega}_{\mathcal{F}_3^u} = \int d\mu \left( -\frac{\bar{\Omega}_{\mathcal{F}_3^u}}{T_2} \right) \\ &= \varepsilon \left[ \frac{1}{X_2 + Y_1 + 2Y_2} \bar{\Omega}_{\mathcal{F}_3^u} + \left( \frac{1}{X_1 + X_2} - \frac{1}{X_2 + Y_1 + 2Y_2} \right) \bar{\Omega}_{\mathcal{Q}_3} \right], \end{aligned} \quad (\text{A.14b})$$

$$\begin{aligned} \partial_{Y_1} \mathcal{F}_3^u &= \int d\mu \left[ \partial_{x_1} \left( \frac{x_1}{X_1 - Y_1 - 2Y_2} \bar{\Omega}_{\mathcal{F}_3^u} \right) + \partial_{x_2} \left( \frac{x_2 + X_1 + X_2}{X_1 - Y_1 - 2Y_2} \bar{\Omega}_{\mathcal{F}_3^u} \right) \right] \\ &= \varepsilon \left[ \left( \frac{1}{X_2 + Y_1 + 2Y_2} - \frac{1}{X_1 - Y_1 - 2Y_2} \right) \bar{\Omega}_{\mathcal{F}_3^u} - \frac{1}{X_2 + Y_1 + 2Y_2} \bar{\Omega}_{\mathcal{Q}_3} \right], \end{aligned} \quad (\text{A.14c})$$

$$\partial_{Y_2} \mathcal{F}_3^u = 2\partial_{Y_1} \mathcal{F}_3^u. \quad (\text{A.14d})$$

Collectively, the canonical differential equation for  $\mathcal{F}_3^u$  is

$$\begin{aligned} d\mathcal{F}_3^u &= \varepsilon [\mathcal{F}_3^u d\log(X_1 - Y_1 - 2Y_2) + (\mathcal{F}_3^u - \mathcal{Q}_3) d\log(X_2 + Y_1 + 2Y_2) \\ &\quad + \mathcal{Q}_3 d\log(X_1 + X_2)]. \end{aligned} \quad (\text{A.15})$$

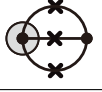
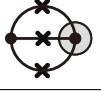





















## B Tubings of Two-Site Two-Loop Bubble System

In Eq. (5.3), we defined the integral family for two-site two-loop bubble correlator  $\mathbf{I}_{\text{sun}}$ , where the functions in  $\mathbf{I}_{\text{sun}}$  can be organized into three distinct hierarchical layers:

Layer-0	Layer-1		Layer-2
	$\mathcal{F}_1$	$\tilde{\mathcal{F}}_1$	$\mathcal{Q}_1$
	$\mathcal{F}_2$	$\tilde{\mathcal{F}}_2$	$\mathcal{Q}_2$
	$\mathcal{F}_3$	$\tilde{\mathcal{F}}_3$	$\mathcal{Q}_3$
$\mathcal{P}$	$\mathcal{F}_4$	$\tilde{\mathcal{F}}_4$	$\mathcal{Q}_4$
	$\mathcal{F}_5$	$\tilde{\mathcal{F}}_5$	$\mathcal{Q}_5$
	$\mathcal{F}_6$	$\tilde{\mathcal{F}}_6$	$\mathcal{Q}_6$
	$\mathcal{F}_7$	$\tilde{\mathcal{F}}_7$	$\mathcal{Q}_7$

(B.1)

Further, we have derived the canonical differential equations associated with  $\mathbf{I}_{\text{sun}}$  as summarized in Eq. (5.4), where all the letters appearing in the DEs are defined in the table below:

$l_1$		$\text{dlog}(X_1 + Y_1 + Y_2 + Y_3)$	$l_2$		$\text{dlog}(X_2 + Y_1 + Y_2 + Y_3)$
$l_3$		$\text{dlog}(X_1 + Y_1 + Y_2 - Y_3)$	$l_4$		$\text{dlog}(X_2 + Y_1 + Y_2 - Y_3)$
$l_5$		$\text{dlog}(X_1 + Y_1 - Y_2 + Y_3)$	$l_6$		$\text{dlog}(X_2 + Y_1 - Y_2 + Y_3)$
$l_7$		$\text{dlog}(X_1 - Y_1 + Y_2 + Y_3)$	$l_8$		$\text{dlog}(X_2 - Y_1 + Y_2 + Y_3)$
$l_9$		$\text{dlog}(X_1 + Y_1 - Y_2 - Y_3)$	$l_{10}$		$\text{dlog}(X_2 + Y_1 - Y_2 - Y_3)$
$l_{11}$		$\text{dlog}(X_1 - Y_1 + Y_2 - Y_3)$	$l_{12}$		$\text{dlog}(X_2 - Y_1 + Y_2 - Y_3)$
$l_{13}$		$\text{dlog}(X_1 - Y_1 - Y_2 + Y_3)$	$l_{14}$		$\text{dlog}(X_2 - Y_1 - Y_2 + Y_3)$
$l_{15}$		$\text{dlog}(X_1 - Y_1 - Y_2 - Y_3)$	$l_{16}$		$\text{dlog}(X_2 - Y_1 - Y_2 - Y_3)$
$l_{17}$		$\text{dlog}(X_1 + X_2 + 2Y_1 + 2Y_2)$	$l_{18}$		$\text{dlog}(X_1 + X_2 + 2Y_1 + 2Y_3)$
$l_{19}$		$\text{dlog}(X_1 + X_2 + 2Y_2 + 2Y_3)$	$l_{20}$		$\text{dlog}(X_1 + X_2 + 2Y_1)$
$l_{21}$		$\text{dlog}(X_1 + X_2 + 2Y_2)$	$l_{22}$		$\text{dlog}(X_1 + X_2 + 2Y_3)$
$l_{23}$		$\text{dlog}(X_1 + X_2)$			

**Table 3.** The alphabet for two-site two-loop sunset-type wavefunction coefficient where the letters  $l_i = \text{dlog}(w_i)$ .



## References

- [1] N. Arkani-Hamed, P. Benincasa, and A. Postnikov, “Cosmological Polytopes and the Wavefunction of the Universe,” [arXiv:1709.02813 \[hep-th\]](#).
- [2] N. Arkani-Hamed and P. Benincasa, “On the Emergence of Lorentz Invariance and Unitarity from the Scattering Facet of Cosmological Polytopes,” [arXiv:1811.01125 \[hep-th\]](#).
- [3] P. Benincasa, “From the flat-space S-matrix to the Wavefunction of the Universe,” [arXiv:1811.02515 \[hep-th\]](#).
- [4] P. Benincasa, “Cosmological Polytopes and the Wavefunction of the Universe for Light States,” [arXiv:1909.02517 \[hep-th\]](#).
- [5] S. De and A. Pokraka, “Cosmology meets cohomology,” *JHEP* **03** (2024) 156, [arXiv:2308.03753 \[hep-th\]](#).
- [6] P. Benincasa, G. Brunello, M. K. Mandal, P. Mastrolia, and F. Vazão, “On one-loop corrections to the Bunch-Davies wavefunction of the universe,” [arXiv:2408.16386 \[hep-th\]](#).
- [7] N. Arkani-Hamed, D. Baumann, A. Hillman, A. Joyce, H. Lee, and G. L. Pimentel, “Kinematic Flow and the Emergence of Time,” [arXiv:2312.05300 \[hep-th\]](#).
- [8] N. Arkani-Hamed, D. Baumann, A. Hillman, A. Joyce, H. Lee, and G. L. Pimentel, “Differential Equations for Cosmological Correlators,” [arXiv:2312.05303 \[hep-th\]](#).
- [9] K. Aomoto, “On vanishing of cohomology attached to certain many valued meromorphic functions,” *Journal of the Mathematical Society of Japan* **27** no. 2, (1975) 248–255.
- [10] K. Aomoto and M. Kita, *Theory of Hypergeometric Functions*. Springer Monographs in Mathematics. Springer, 2011.
- [11] P. Mastrolia and S. Mizera, “Feynman Integrals and Intersection Theory,” *JHEP* **02** (2019) 139, [arXiv:1810.03818 \[hep-th\]](#).
- [12] J. M. Henn, “Multiloop integrals in dimensional regularization made simple,” *Phys. Rev. Lett.* **110** (2013) 251601, [arXiv:1304.1806 \[hep-th\]](#).
- [13] J. M. Henn, “Lectures on differential equations for Feynman integrals,” *J. Phys. A* **48** (2015) 153001, [arXiv:1412.2296 \[hep-ph\]](#).
- [14] M. Carr and S. L. Devadoss, “Coxeter complexes and graph-associahedra,” *Topology and its Applications* **153** no. 12, (2006) 2155–2168.
- [15] S. L. Devadoss and M. Smith, “Colorful graph associahedra,” [arXiv:2011.08169](#).
- [16] P.-H. Balduf, A. Cantwell, K. Ebrahimi-Fard, L. Nabergall, N. Olson-Harris, and K. Yeats, “Tubings, chord diagrams, and dyson–schwinger equations,” *Journal of the London Mathematical Society* **110** no. 5, (2024) e70006.
- [17] S. He, X. Jiang, J. Liu, Q. Yang, and Y.-Q. Zhang, “Differential equations and recursive solutions for cosmological amplitudes,” *JHEP* **01** (2025) 001, [arXiv:2407.17715 \[hep-th\]](#).
- [18] N. Arkani-Hamed, Y. Bai, and T. Lam, “Positive Geometries and Canonical Forms,” *JHEP* **11** (2017) 039, [arXiv:1703.04541 \[hep-th\]](#).
- [19] A. B. Goncharov, M. Spradlin, C. Vergu, and A. Volovich, “Classical Polylogarithms for Amplitudes and Wilson Loops,” *Phys. Rev. Lett.* **105** (2010) 151605, [arXiv:1006.5703 \[hep-th\]](#).

- [20] C. Duhr, H. Gangl, and J. R. Rhodes, “From polygons and symbols to polylogarithmic functions,” *JHEP* **10** (2012) 075, [arXiv:1110.0458 \[math-ph\]](#).
- [21] C. Duhr and F. Dulat, “PolyLogTools — polylogs for the masses,” *JHEP* **08** (2019) 135, [arXiv:1904.07279 \[hep-th\]](#).
- [22] A. Hillman, “Symbol Recursion for the dS Wave Function,” [arXiv:1912.09450 \[hep-th\]](#).
- [23] F. Gasparotto, P. Mazloumi, and X. Xu, “Differential equations for tree-level cosmological correlators with massive states,” [arXiv:2411.05632 \[hep-th\]](#).